Nat Hazards (2017) 87:1189–1222
DOI 10.1007/s11069-017-2815-5

ORIGINAL PAPER

Numerical simulation of the 30–45 ka debris avalanche flow of Montagne Pelée volcano, Martinique: from volcano flank collapse to submarine emplacement

Morgane Brunet[1] · Laurent Moretti[1] · Anne Le Friant[1] · Anne Mangeney[1,2] · Enrique Domingo Fernández Nieto[3] · Francois Bouchut[4]

Received: 14 June 2016 / Accepted: 10 March 2017 / Published online: 6 April 2017
© Springer Science+Business Media Dordrecht 2017

Abstract We simulate here the emplacement of the debris avalanche generated by the last flank collapse event of Montagne Pelée volcano (30–45 ka), Martinique, Lesser Antilles. Our objective is to assess the maximum distance (i.e., runout) that can be reached by this type of debris avalanche as a function of the volume involved. Numerical simulations are performed using two complementary depth-averaged thin-layer continuum models because no complete models were available in the literature. The first model, SHALTOP, accurately describes dry granular flows over a 3D topography and may be easily extended to describe submarine avalanches. The second model, HYSEA, describes the subaerial and submarine parts of the avalanche as well as its interaction with the water column. However, HYSEA less accurately describes the thin-layer approximation on the 3D topography. Simulations were undertaken testing different empirical friction laws and debris avalanche volume flows. Our study suggests that large collapses ($\sim$25 km^3) probably occurred in several times with successive volumes smaller than about 5 km^3 entering the sea. This result provides new constraints on the emplacement processes of debris avalanches associated with these collapses which can drastically change the related hazard assessment such as the generated tsunami, in a region known for its seismic and volcanic risks.

Keywords Numerical modeling · Volcano flank collapse · Montagne Pelée volcano · Martinique · Debris avalanche deposit

✉ Morgane Brunet
mbrunet@ipgp.fr

[1] Laboratoire des Systèmes Volcaniques, Institut de Physique du Globe de Paris, Sorbonne Paris Cité, CNRS UMR 7154, 1, rue Jussieu, 75238 Paris, France

[2] ANGE Team, CEREMA, INRIA, Lab. J. Louis Lions, Paris, France

[3] Departamento Matemática Aplicada I, E.T.S. Arquitectura, Universidad de Sevilla, Sevilla, Spain

[4] Laboratoire d'Analyse et de Mathématiques Appliquées, CNRS, UPEM, UPEC, Université Paris-Est Marne-la-Vallée, Champs-sur-Marne, France

1 Introduction

Volcano flank collapse is recognized as a recurrent process into the long-term evolution of a volcanic edifice (Siebert 1984; McGuire 1996). These processes produce typical horse-shoe-shaped structures on-land and debris avalanche deposits with a typical hummocky morphology. The most important mass-wasting deposits have been recognized offshore volcanic islands where they can extend up to several tens of kilometers away from the coastline, such as in Hawaii (Moore et al. 1989; Moore et al. 1994), the Canary Islands (Carracedo 1999; Masson et al. 2002), La Réunion Island (Labazuy 1996; Oehler et al. 2008; Le Friant et al. 2011) or the Lesser Antilles (Deplus et al. 2001; Le Friant et al. 2003a; Boudon et al. 2007). Such deposits emplacement into the sea can also trigger catastrophic tsunamis (e.g., Harbitz et al. 2012). Currently, it remains unclear how debris avalanche emplaces from subaerial to submarine environments because of monitoring difficulties or absence of observations and significant uncertainties concerning submarine dynamics and its modeling.

The IODP expedition 340 (March 3–April 17, 2012) provides for the first time some drilling through the large landslide deposits offshore Lesser Antilles volcanoes (Le Friant et al. 2013, 2015). Drilled cores data were combined with seismic reflection data from three different cruises (AGUADOMAR 1999; CARAVAL 2002 and GWADASEIS 2009) to reinterpret the composition and emplacement dynamics of large mass-wasting deposits recognized offshore Montserrat and Martinique in the Lesser Antilles. For instance, the larger landslide deposit recognized that offshore the island (Fig. 1a, light-gray SLD deposit, runout distance $\sim$70 km) is not composed of volcanic debris avalanche deposit but results from seafloor sediment failure (Brunet et al. 2016). Le Friant et al. (2015) and Brunet et al. (2016) propose that flank collapse of Montagne Pelée volcano in Martinique produced debris avalanches that flowed down the volcanic edifice and submarine volcano slope until the Grenada Basin. At this transition location (i.e., between the submarine volcano slope and "flat" Grenada Basin at 30–35 km from the coastline), the debris avalanche lost inertia, slowed down and deposited (Fig. 1a, dark DAD deposits, runout distance $\sim$30 km). This new scenario implies shorter runout distance of debris avalanche than previously proposed (Deplus et al. 2001; Le Friant et al. 2003a; Boudon et al. 2007) and has consequences on the understanding of their dynamics. To confirm this scenario, key questions remain about the emplacement process: is there a critical runout distance reached by these flows, what is the influence of the transition between submarine volcano flank and Grenada Basin? How does the water or initial collapse volume control this runout distance? What is the dynamics of debris avalanches in this region? Do the flank collapse events occur in one time or in several phases? The latter implies the flow of smaller debris avalanche volumes.

The aim of this paper is to address these questions to better constrain this new scenario. To do so, we perform numerical simulations of aerial to submarine debris avalanches emplacement related to Montagne Pelée flank collapse in Martinique. Our numerical simulations focused on the last major flank collapse event recognized on Montagne Pelée volcano. Numerical modeling of subaerial debris avalanches has been significantly developing since the pioneered work of Savage and Hutter (1989). Since then, a great number of studies investigated volcano flank collapse and associated debris avalanches with numerical simulations using different numerical models to reproduce specific debris avalanches events (Gittings 1992; Kelfoun et al. 2011; Abadie et al. 2008, 2010; Heinrich et al. 2001a, b; Mangeney et al. 2000; Kelfoun and Vargas 2015). In this study based on

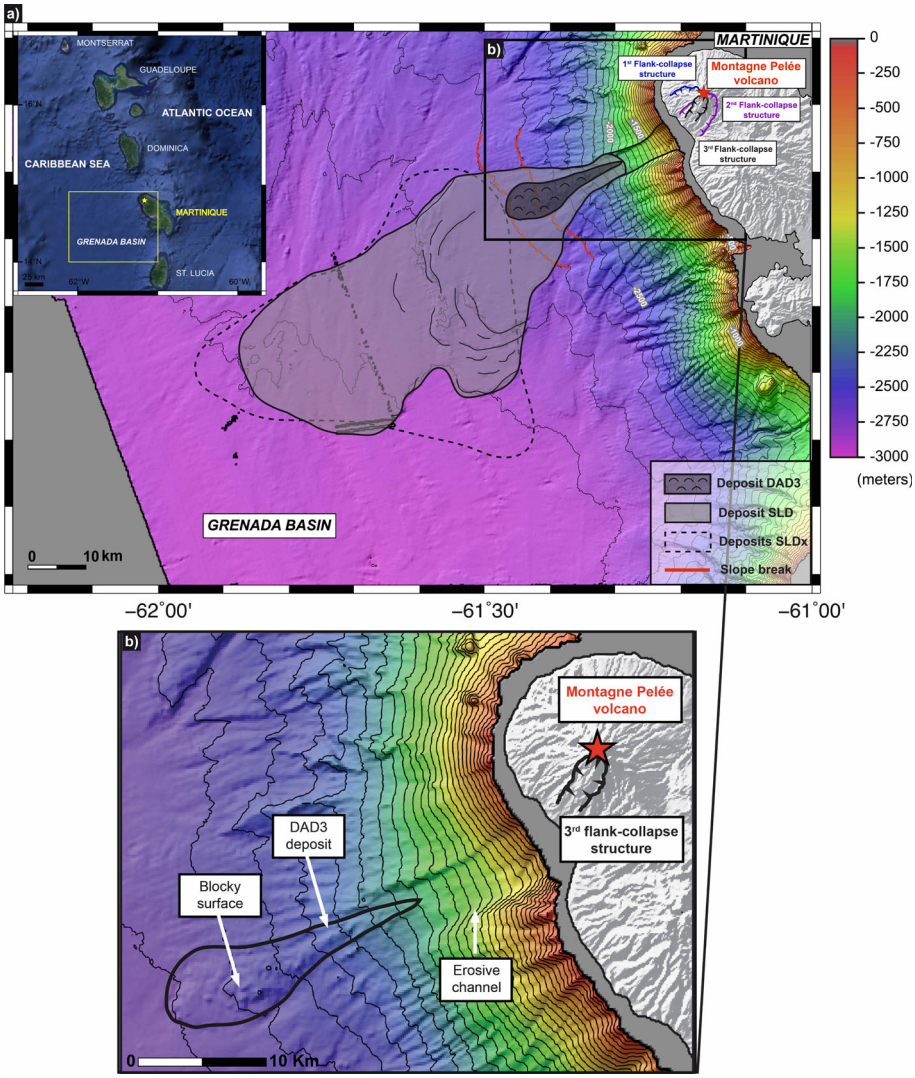

Fig. 1 **a** Terrestrial digital elevation model (from IGN) with Montagne Pelée volcano (*red star*) and bathymetric map from the AGUADOMAR (1999) and CARAVAL (2002) cruises. The three horseshoe-shaped structures are represented (Le Friant et al. 2003a). Submarine landslide deposit extents inferred are illustrated (*black lines*, Brunet et al. 2016). *Inset* Lesser Antilles Arc map on the left-hand side, with Martinique Island (*yellow star*). **b** Zoom on the northwest part of Martinique, highlighting the last flank collapse event of Montagne Pelée volcano with the flank collapse structure on-land and the DAD3 debris avalanche deposit offshore

one specific event, we test different physical parameter in order to better understand their impact on debris avalanche emplacement. To do so, our simulations based on the accurate description of an arbitrary complex 3D topography within thin-layer depth-averaged models are now possible (e.g., Bouchut et al. 2003; Bouchut and Westdickenberg 2004; Mangeney-Castelnau et al. 2007). This description involves the full tensor of the topography curvature as implemented in the SHALTOP model, while most of the other models

only use part of the curvature terms thus neglecting some centrifugal forces. These forces may, however, play a key role in the avalanche dynamics (Favreau et al. 2010; Moretti et al. 2015). On the other hand, submarine avalanche models have been poorly developed. The physical processes involved (granular–fluid interaction, dilatancy effects, etc.) and their description within the thin-layer depth-averaged approximation are still challenging (e.g., Abadie et al. 2011, 2012; Harris et al. 2012; Pitman and Le 2005; Fernandez-Nieto et al. 2008; Pelanti et al. 2008; Pailha and Pouliquen 2009; Kelfoun 2011; Iverson and George 2014; Bouchut et al. 2015a, b; Delannay et al. 2016). Furthermore, the description of topography effects in these models is not accurate [e.g., oversimplified projection of gravity terms in Le Friant et al. (2003b), thin-layer approximation applied in the horizontal/vertical reference frame in Fernandez-Nieto et al. (2008)]. As a result, up to now there is no model that properly accounts for both granular/fluid interaction and topography effects. In this context, we propose to combine (1) an accurate dry granular flow model (SHALTOP) and its simple extension to submarine flow in order to reflect properly topography effects and (2) a submarine avalanche model (HYSEA) in order to better assess the effect of water on granular flow mobility. The ultimate goal is to investigate the order of magnitude of the runout distance that the Montagne Pelée major debris avalanches could reach as a function of the volume involved and thus confirm or question the conceptual scenario proposed by Brunet et al. (2016).

Previous numerical simulations of the last debris avalanche of Montagne Pelée volcano have been carried out by Le Friant et al. (2003b) using a thin-layer depth-averaged numerical model, solving mass and momentum conservation equations for a frictional granular material (generally called Saint-Venant or Savage–Hutter equations). The Savage–Hutter model (1989) involves two friction angles: the basal friction angle and the internal friction angle. Sensitivity analysis shows that the internal friction angle plays a smaller role on the avalanche dynamics and deposit than the basal friction angle (see, e.g., Pirulli and Mangeney 2008). Le Friant et al. (2003b) considered either the Coulomb friction law with a constant friction coefficient or the so-called Pouliquen friction law (e.g., Pouliquen, 1999) where the friction coefficient depends on the strain rate and pressure (i.e., on the velocity and thickness of the flow). The authors concluded that Pouliquen friction law (1999) best reproduces the debris avalanche deposit emplacement, using friction angles between 6° and 15°. However, up to now, no rigorous asymptotic development of the thin-layer depth-averaged model over an arbitrary topography including the internal friction angle has been proposed. As a result, we ignore here the internal friction angle and consider the friction coefficient in the model as an effective friction coefficient describing the mean dissipation during the flow, whose value is obtained empirically by fitting the observed deposit (e.g., Lucas et al. 2014). Therefore, we extend here the simulations of Le Friant et al. (2003b) by using more accurate numerical models and test different scenario.

In the first section, we describe the last debris avalanche deposit characteristics of Montagne Pelée volcano and the numerical models used in this study. In the second section, we present a series of sensitivity tests. First, simulations with the SHALTOP numerical model were performed using the same rheological behavior and parameters as in Le Friant et al. (2003b), such as the Coulomb and Pouliquen friction laws with friction angles values between 6° and 15°. Then, simulations with SHALTOP were carried out using the Coulomb friction law and different Pouliquen friction laws considering four friction angles as in Pouliquen and Forterre (2002). Finally, using the best agreement in terms of friction law and friction angles, simulations were carried out with the HYSEA numerical model. All simulations were systematically performed in both dry and wet conditions. In the last and third section, we compare and discuss results in order to

highlight the influence of each physical parameter (water, friction law, friction angles and mass flow volumes) on the runout distance and morphology of the debris avalanche deposit. These simulations together with observed deposits give new constraints on the debris avalanche emplacement process and volume of past collapse events.

2 Geological context and data

2.1 The 30–45 ka flank collapse event and resulting DAD3 deposit

Montagne Pelée volcano in Martinique (Lesser Antilles arc, Fig. 1a) has experienced three major flank collapse events during the last ~130 ka years, which removed several km^3 to tens of km^3 of the western flank of the volcano (Le Friant et al. 2003a; Boudon et al. 2005, 2007). Each of these flank collapses produced a horseshoe-shaped structure on the volcano (Fig. 1b) and generated debris avalanches that flowed into the Caribbean Sea. The first major flank collapse was dated as older than 127 ka with a collapse volume of 25 km^3 (Germa et al. 2011; Le Friant et al. 2003a). The second major flank collapse was dated between 45 and 127 ka with a collapse volume of 13 km^3 (Le Friant et al. 2015). Finally, the last major flank collapse was dated between 45 and 30 ka with a collapse volume of 1.8 km^3 (Le Friant et al. 2015). We focus here on the last-recognized flank collapse event in order to better understand debris avalanche emplacement dynamics (Fig. 1b).

The last-recognized flank collapse event triggered a debris avalanche that flowed into the sea forming the submarine DAD3 deposit. This event corresponds to the smallest one, with an on-land structure of 1.5 × 4 km and a missing volume of 1.8 km^3 (Fig. 1b). Offshore, the DAD3 deposit was 1.8 km^3, covering an area of 50 km^2 with an average thickness of about 10 to 15 m, but it reaches locally 20–30 m. It extends over ~30 km from the coastline and is located at the base of an erosive channel, with slopes between 10° and 20° close to shoreline and less than 5° further downslope the submarine flank, around 30–35 km off the coast. It displays a typical hummocky morphology and an elongated shape with a morphological front at its frontal edge (Fig. 1b). Megablocks 100–500 m in diameter and 10–40 m high are concentrated in the central part of the deposit (Fig. 1b) (Le Friant et al. 2003b).

2.2 Data

Swath bathymetry collected during the AGUADOMAR cruise (Deplus et al. 2001) was used to build a 50-m resolution digital terrain model (Fig. 1). To reconstruct topography of the volcano before failure, Le Friant et al. (2003b) altered the DTM: (1) the submarine debris avalanche deposit was removed and replaced by a smooth slope; (2) the landslide volume in its assumed initial position was defined by a parabolic-shaped volume of 1.8 km^3. The SHALTOP numerical model used to perform the simulations requires smooth enough topography fluctuations, and the radius of curvature has to be larger than the thickness of the avalanche. Violating this condition means to leave the range of validity of the model and induces instabilities. Because of this, the DTM from Le Friant et al. (2003b) was smoothed. It has been done by calculating the mean value of the topography over a sliding window containing the 24 closest points. To obtain our final rough topography, we performed 20 times this procedure. Thus, numerical simulations were carried out with both a smooth and an artificial roughness topography, by adding random topography

fluctuations where Le Friant et al. (2003b) had removed the DAD3 deposit, in order to consider a more realistic topography. This roughness is characterized by a lateral amplitude of 1–1.5 km large, a vertical amplitude of 11 m high in average, with a minimum of 7 m and a maximum of 15 m, typical of the surrounding roughness. Further studies should be performed to precisely study the effect of roughness on the simulations, which is beyond the scope of this paper. Furthermore, different collapse volumes have been tested to investigate the possible relationship between volumes and runout distance. To do this, we defined initial collapsing mass with a 3D parabolic shape characterized by its height (H_0) and width (W_0). To change the associated volume, we varied either the height H_0 of the parabola while keeping a fixed width W_0 or its width with a fixed height. The avalanche is treated as a homogeneous and incompressible continuum, i.e., it does not take into account explicitly the presence of pore fluids, bed erosion, density variation due to expansion of the material and possible incorporation of air or water.

3 Numerical models

Debris avalanches, composed of particles with sizes ranging from millimeters to several hundred meters, are generally very heterogeneous. However, this heterogeneity is hard to describe in models able to simulate avalanches at the natural scale. The avalanche is treated here, as classically done, as a homogeneous and incompressible continuum. In particular, we do not take into account density variation due to expansion or contraction of the material and its impacts on pore fluid pressure, segregation and fragmentation processes, bed erosion or incorporation of air or water (Delannay et al. 2016).

3.1 The SHALTOP numerical model

As a first step, we use the SHALTOP numerical model (Bouchut et al. 2003; Bouchut and Westdickenberg 2004; Mangeney-Castelnau et al. 2005; Mangeney et al. 2007b) that allows to simulate dry granular flows on complex topographies. One of the strengths of this model is that it involves a single free parameter: the friction coefficient $\mu = \tan\delta$, where δ is the friction angle. Following the approach of Savage and Hutter (1989), mass and momentum conservation equations are depth averaged over the flow thickness, considering that the flowing thickness in the direction normal to the topography is much smaller than the characteristic flow length along the slope. SHALTOP takes into account the curvature tensor, contrary to the existing models (e.g., Le Friant et al. 2003b; Hungr 2008), to our knowledge.

$$H = c^3 \begin{pmatrix} \dfrac{\partial^2 b}{\partial x^2} & \dfrac{\partial^2 b}{\partial x \partial y} \\ \dfrac{\partial^2 b}{\partial x \partial y} & \dfrac{\partial^2 b}{\partial y^2} \end{pmatrix} \tag{1}$$

with all its components (Bouchut and Westdickenberg 2004). Here x and y are the horizontal coordinates, and the topography is described by the scalar function $b(x, y)$ with a 3D unit upward normal vector.

$$\vec{n} = \left(\frac{-\nabla_x b}{\sqrt{1 + \|\nabla_x b\|^2}}, \quad \frac{1}{\sqrt{1 + \|\nabla_x b\|^2}} \right) = (-s, c) \in \mathbb{R}^2 \times \mathbb{R}. \tag{2}$$

where $\boldsymbol{x} = (x, y) \in \mathbb{R}^2$, the scalar $c = \cos\theta$ is the cosine of the angle between the vertical direction and the normal $\vec{n}$. In our notation, the 3D vectors are denoted by $\vec{.}$, whereas the 2D vectors are written in bold.

The flow is described by

$$h(t, \boldsymbol{x}) \geq 0, \quad \boldsymbol{u}'(t, \boldsymbol{x}) \in \mathbb{R}^2, \tag{3}$$

where h is the thickness of the avalanche in the direction normal to the topography and $\boldsymbol{u}' = (u, u_t)$ is a parameterization of the velocity. This parameterization has been defined in order to simplify the equations with topography. The real 3D material velocity has horizontal/vertical components.

$$\vec{u} = (c\boldsymbol{u}', \quad \boldsymbol{s} \cdot \boldsymbol{u}') \tag{4}$$

This physical velocity is tangent to the topography, $\vec{u} \cdot \vec{n} = 0$, as would be expected for shallow flows. In the horizontal Cartesian coordinate formulation, the model can be expressed as

$$\partial_t(h/c) + \nabla_x \cdot (h\boldsymbol{u}') = 0 \tag{5}$$

$$\begin{aligned} &\partial_t \boldsymbol{u}' + cu' \cdot \nabla_x \boldsymbol{u}' + \frac{1}{c}(Id - \boldsymbol{s}\boldsymbol{s}^t)\nabla_x(g(hc + b)) = \\ &\frac{-1}{c}(\boldsymbol{u}'^t H \boldsymbol{u}')\boldsymbol{s} + \frac{1}{c}(\boldsymbol{s}^t H \boldsymbol{u}')\boldsymbol{u}' - \frac{g\mu c\boldsymbol{u}'}{\sqrt{c^2\|\boldsymbol{u}'\|^2 + (\boldsymbol{s} \cdot \boldsymbol{u}')^2}} \left(1 + \frac{\boldsymbol{u}'^t H \boldsymbol{u}'}{gc}\right)_+ \end{aligned} \tag{6}$$

where ∇_x is the gradient vector in the horizontal (x, y) plane and g the acceleration due to gravity. The subscript $+$ stands for the positive part, $x_+ = \max(0, x)$ (see Bouchut and Westdickenberg 2004 and Mangeney-Castelnau et al. 2007 for more details). The rheological behavior is described by a Coulomb-type friction law involving a constant or variable friction coefficient μ (see Sect. 3.3 for more details).

Note that replacing the gravity g by κg, with

$$\kappa = 1 - \rho_w/\rho_s \tag{7}$$

makes it possible to recover the submarine flow equations when the coupling between the avalanche and the water column is neglected (see next Sect. 3.2).

3.2 The HYSEA numerical model

The 1D HYSEA model proposed by Fernandez-Nieto et al. (2008) is a two-layer 1D model developed to simulate submarine avalanches. One layer represents the granular avalanche modeled as in Savage and Hutter (1989), and the upper layer represents the fluid. As the granular avalanche layer, the fluid layer is assumed to be thin.

We use here the 2D HYSEA model corresponding to a 2D extension of the model proposed in Fernandez-Nieto et al. (2008). The unknowns of the problem are the heights and the velocities of the fluid and of the granular layers. The main simplification in the current version of the 2D extension of the model is to make the thin-layer approximation in

the Cartesian reference frame (i.e., horizontal/vertical). This leads to assume that the thickness of the flow in the vertical direction is much smaller than the horizontal flow extension and that the velocity is mostly horizontal. This is much less accurate than what is assumed in the granular model of Savage and Hutter (1989) and in SHALTOP where the thickness in the direction normal to the flow is assumed to be small compared to the downslope extension of the flow and that the velocity is almost tangent to the topography. However, contrary to SHALTOP, 2D HYSEA takes into account the interaction between the avalanche and water. In both models, the buoyancy effects are taken into account but only the drag force between the free surface of the landslide and the ocean layer is not simulated in SHALTOP while it is simulated in HYSEA. Note that HYSEA model also makes it possible to simulate the tsunami generated by the submarine avalanche.

With subindex 1 let us denote the unknowns corresponding to the fluid layer: h_1 is the height and $\boldsymbol{u}_1$ the velocity vector of the fluid layer. Index 2 corresponds to the granular layer: h_2 is the height and $\boldsymbol{u}_2$ the velocity of the granular layer.

The mass and momentum conservation equations are:

$$\begin{aligned}
&\partial_t h_1 + \nabla_x \cdot (h_1 \boldsymbol{u}_1) = 0,\\
&\partial_t \boldsymbol{u}_1 + u_1 \cdot \nabla_x u_1 + \nabla_x (g(b + h_1 + h_2)) = \beta(\boldsymbol{u}_2 - \boldsymbol{u}_1),\\
&\partial_t h_2 + \nabla_x \cdot (h_2 \boldsymbol{u}_2) = 0,\\
&\partial_t u_2 + \boldsymbol{u}_2 \cdot \nabla_x \boldsymbol{u}_2 + \nabla_x (g(b + h_2 + (1-\kappa)h_1)) = -\beta(\boldsymbol{u}_2 - \boldsymbol{u}_1) - g\kappa\mu \frac{\boldsymbol{u}_2}{\|\boldsymbol{u}_2\|}.
\end{aligned} \tag{8}$$

where $\beta(\boldsymbol{u}_2 - \boldsymbol{u}_1)$ defines the friction term between the fluid and the granular layers. Moreover, note that if we assume that the free surface is nearly horizontal, that is,

$$\nabla_x (b + h_1 + h_2) = 0, \tag{9}$$

we can simplify the velocity equation for the granular layer. Indeed, by using $\nabla_x h_1 = -\nabla_x (b + h_2)$ we obtain the system

$$\begin{cases}
\partial_t h_1 + \nabla_x \cdot (h_1 \boldsymbol{u}_1) = 0,\\
\partial_t \boldsymbol{u}_1 + \boldsymbol{u}_1 \cdot \nabla_x \boldsymbol{u}_1 + \nabla_x (g(b + h_1 + h_2)) = \beta(\boldsymbol{u}_2 - \boldsymbol{u}_1),\\
\partial_t h_2 + \nabla_x \cdot (h_2 \boldsymbol{u}_2) = 0,\\
\partial_t \boldsymbol{u}_2 + \boldsymbol{u}_2 \cdot \nabla_x \boldsymbol{u}_2 + \nabla_x (g\kappa(b + h_2)) = -\beta(\boldsymbol{u}_2 - \boldsymbol{u}_1) - g\kappa\mu \frac{u_2}{\|\boldsymbol{u}_2\|}.
\end{cases} \tag{10}$$

Finally, let us remark that if the friction between the fluid and the granular layer is neglected, the system describing the evolution of the granular layer can be decoupled from the evolution of the fluid layer. The granular layer evolution can be obtained as the solution of the following system

$$\begin{cases}
\partial_t h_2 + \nabla_x \cdot (h_2 \boldsymbol{u}_2) = 0,\\
\partial_t \boldsymbol{u}_2 + \boldsymbol{u}_2 \cdot \nabla_x \boldsymbol{u}_2 + \nabla_x (g\kappa(b + h_2)) = -g\kappa\mu \frac{u_2}{\|\boldsymbol{u}_2\|}.
\end{cases} \tag{11}$$

This corresponds to Eqs. (5), (6), implemented in SHALTOP when substituting the gravity acceleration g by κg and with the simplification $c = 1$, $s = 0$, $H = 1$. Indeed, when the friction between the fluid and granular layers is neglected, the effect of water only plays a role in the acceleration terms (divide Eq. (11) by κ).

3.3 Friction laws

We test here the Coulomb and three versions of the Pouliquen friction laws proposed in the literature.

3.3.1 The Coulomb friction law

Following Lucas et al. (2014), we use the Coulomb friction law with a constant friction coefficient μ:

$$\mu = \tan\delta. \tag{12}$$

where δ is the constant so-called basal friction angle. This is the simpler friction law that can be used in landslide models making it possible to have only one parameter to constrain empirically. We assume here that all the dissipation is empirically taken into account in the so-called basal friction term involving $\boldsymbol{\mu}$. Indeed, the formulation of the Coulomb friction law including internal and basal friction coefficients in thin-layer depth-averaged models on 3D topography is still an open issue (see, e.g., Denlinger and Iverson 2004; Pudasaini and Hutter 2007).

3.3.2 The Pouliquen friction law (1999)

Pouliquen (1999) argued that a constant friction coefficient does not allow to reproduce steady uniform flows over rough beds observed in the laboratory for a range of inclination angles. To reproduce these flows, he introduced an empirical friction coefficient μ that depends on the norm of the mean velocity u and on the thickness h of the granular layer:

$$\mu(u,h) = \tan\delta_1 + (\tan\delta_2 - \tan\delta_1)\exp\left(-\frac{\beta h}{L}\frac{\sqrt{gh}}{u}\right). \tag{13}$$

where δ_1 and δ_2 are characteristic friction angles of the material. In this expression, L represents the mean size of grains and β is an empirical parameter. This law predicts that the friction coefficient varies between $\tan\delta_1$ and $\tan\delta_2$. Large velocities or small thicknesses lead to high friction coefficients.

To avoid numerical issues when the velocity is close to zero in Eq. (13), we considered a threshold value $u_s = 0.001$ m/s for the velocity. If $u < u_s$, we set $u = u_s$.

3.3.3 The extended Pouliquen friction law (1999)

However, the starting angle for an avalanche to flow is higher than the angle for an avalanche to stop. For these reasons, a different friction coefficient should be used when the mass starts to destabilize from rest at zero velocity, i.e., at zero Froude number $F_r = \frac{u}{\sqrt{gh}} = 0$. This leads to introduce two other friction angles δ_3 and δ_4 that are related to the behavior when starting from rest.

The behavior at $0 < F_r < \beta$ corresponds to metastable conditions, for which the description of the mechanical behavior is still uncertain. An empirical ad hoc fit has been proposed by Pouliquen and Forterre (2002) to relate the behavior at $F_r > \beta$, to the measurements at $F_r = 0$. We used it to extend the friction law (13):

- If $F_r \geq \beta$:

$$\mu(h,u) = \tan\delta_1 + (\tan\delta_2 - \tan\delta_1)\exp\left(-\frac{\beta h}{L}\frac{\sqrt{gh}}{u}\right) \tag{14}$$

- If $F_r = 0$:

$$\mu(h) = \mu_{\text{start}}(h) = \tan\delta_3 + (\tan\delta_4 - \tan\delta_3)\exp\left(-\frac{h}{L}\right) \tag{15}$$

- If $0 \leq F_r \leq \beta$:

$$\mu(h,u) = \mu_{\text{start}}(h) + \left(\frac{F_r}{\beta}\right)^{\gamma}(\mu_{\text{stop}}(h) - \mu_{\text{start}}(h)) \tag{16}$$

with

$$\mu_{\text{stop}}(h) = \tan\delta_1 + (\tan\delta_2 - \tan\delta_1)\exp\left(-\frac{h}{L}\right) \tag{17}$$

where γ is an empirical parameter.

3.3.4 The Pouliquen and Forterre friction law (2002)

Pouliquen and Forterre (2002) proposed another shape of these empirical relations:

- If $F_r \geq \beta$:

$$\mu(h,u) = \tan\delta_1 + (\tan\delta_2 - \tan\delta_1)\frac{1}{1 + \frac{\beta h}{L}\frac{\sqrt{gh}}{u}} \tag{18}$$

- If $F_r = 0$:

$$\mu(h) = \mu_{\text{start}}(h) = \tan\delta_3 + (\tan\delta_4 - \tan\delta_3)\frac{1}{1 + \frac{h}{L}} \tag{19}$$

- If $0 \leq F_r \leq \beta$:

$$\mu(h,u) = \mu_{\text{start}}(h) + \left(\frac{F_r}{\beta}\right)^{\gamma}(\mu_{\text{stop}}(h) - \mu_{\text{start}}(h)) \tag{20}$$

with

$$\mu_{\text{stop}}(h) = \tan\delta_1 + (\tan\delta_2 - \tan\delta_1)\frac{1}{1 + \frac{h}{L}} \tag{21}$$

For all the Pouliquen friction laws, when the height h decreases and the velocity increases, the friction increases and vice versa. For all these laws we set $\beta = 0.136$, $L = 1$ m, and $\gamma = 10^{-3}$. For $\gamma < 10^{-2}$ the results are not significantly affected by the value of γ (Pouliquen and Forterre 2002). The friction angles δ_i with $i = 1$–4 will be varied in the following by keeping a constant difference between these angles.

4 Results

Several sensitivity tests have been performed with the SHALTOP model. First, we used the same friction laws and same values of friction angles as those used by Le Friant et al. (2003b). Then the best values of friction angles for each simulation are calibrated numerically on the basis of the best agreement with the following observations: the shape of the submarine deposit (thickness, lateral and longitudinal extensions), the volume of the offshore deposits (1.8 km^3), the runout distance (30 km from the coastline) and the formation of a morphological front (10–20 m) (Fig. 2a). For the last two criteria, the parameters of the flow law are chosen when results and observations do not differ by more than 20%. We quantified the difference between the simulated and observed thickness distribution to identify the best simulations (see Eq. (2) and Table 2). No attempt was made to reproduce the hummocky morphology of the deposits. The height of the initially release mass H_0 and its width W_0 used for the sensitivity tests were both about 500 m (except for simulations testing different debris avalanche volumes).

4.1 Comparison between previous work (Le Friant et al. 2003b) and simulations using SHALTOP

Le Friant et al. (2003b) have already modeled the last flank collapse event on Montagne Pelée using a numerical model (Heinrich et al. 2001a, b). In this model, the role of water in the submarine avalanche was simply taken into account by multiplying the gravity by $\kappa = 1-\rho_w/\rho_d$ as explained in Sects. 2.1 and 2.2, where $-\rho_w$ (the water density) is 1000 km/m^3 and ρ_d (the mass density) is between 1500 and 2500 kg/m^3. The model used by Le Friant et al. (2003b) oversimplified the projection of gravity terms and did not involve the full tensor of the topography curvature. Le Friant et al. (2003b) concluded that the Pouliquen friction law (1999) (Eq. 13) better reproduces DAD3 deposit than the Coulomb friction law, with friction angles of $\delta_1 = 6^\circ$ and $\delta_2 = 15^\circ$. We used the same friction law and angle values in SHALTOP, with two different values for κ, $\kappa = 1$ or $\kappa = 0.5$ to describe dry or wet granular flow, respectively (Fig. 2b, b′, c, c′, d, d′). No differences are observed on the calculated deposit between "dry" and "wet" simulations, i.e., $\kappa = 1$ and $\kappa = 0.5$. This was expected since κ only changes the acceleration terms as discussed in Sect. 3.2. The runout distance simulated by SHALTOP is systematically lower by ~2–7 km than that calculated by Le Friant et al. (2003b) (white lines in Fig. 2), for both the Coulomb and Pouliquen (1999) friction laws. This difference could result from the differences in the treatment of the topography and in the numerical method between the two models. Indeed, as discussed in introduction SHALTOP describes accurately the topography contrary to the model used by Le Friant et al. (2003b), in particular by including the full curvature tensor of the topography (i.e., all the centrifugal forces). Topography effects can significantly change the dynamics and deposit of the simulated landslide (see, e.g., Favreau et al. 2010; Moretti et al. 2015). As an example, taking into account the centrifugal acceleration related to the terrain curvature in a simple simulation of granular flows over a smooth 2D topography reduces by about 5% the runout distance (Fig. 11 of Mangeney-Castelnau et al. 2003). As a result, to reproduce the same runout distance than SHALTOP with a model ignoring the centrifugal effects would require a larger friction angle. Furthermore, the numerical method used in the two codes is different even though they are both based on finite volume methods. In particular, SHALTOP deals accurately with the transition between the avalanche (where the flow thickness h is not

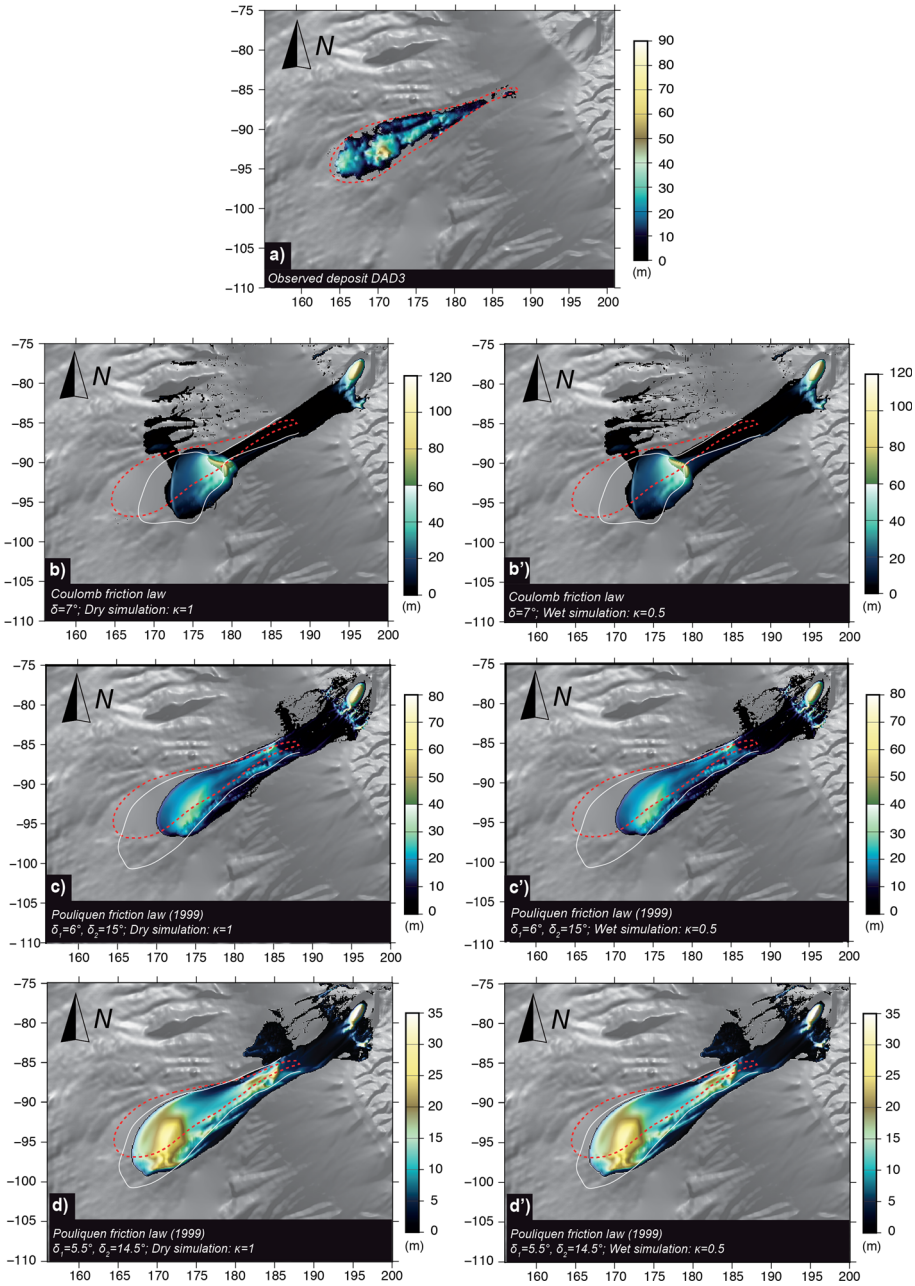

zero) and the topography (where $h = 0$), while the model used in Le Friant et al. (2003b) requires to add a non-physical small thickness on the topography to avoid numerical problems. All these effects could explain the differences observed in the simulation. A detailed description of the numerical methods used in these two codes is, however, beyond the scope of this paper.

◀**Fig. 2** Comparison between Le Friant et al. (2003b) and SHALTOP numerical simulations: Sensitivity tests carried out with the Coulomb and Pouliquen (1999) friction laws using the same values of friction angles as Le Friant et al. (2003b). *Dotted red lines* represent the observed DAD3 deposit extents, white lines illustrate the DAD3 deposit extents calculated by Le Friant et al. (2003b), and the SHALTOP calculated deposit is represented in *color scale*. **a** Topography of the observed DAD3 deposit. **b** Coulomb friction law with $\delta_1 = 7°$ and $\kappa = 1$, **b′** Coulomb friction law with $\delta_1 = 7°$ and $\kappa = 0.5$, **c** Pouliquen friction law (1999) with $\delta_1 = 6°$, $\delta_2 = 15°$ and $\kappa = 1$, **c′** Pouliquen friction law (1999) with $\delta_1 = 6°$, $\delta_2 = 15°$ and $\kappa = 0.5$, **d** Pouliquen friction law (1999) with $\delta_1 = 5.5°$, $\delta_2 = 14.5°$ and $\kappa = 1$, **d′** Pouliquen friction law (1999) with $\delta_1 = 5.5°$, $\delta_2 = 14.5°$ and $\kappa = 0.5$. No differences are observed between dry and wet conditions

4.2 Sensitivity tests using SHALTOP

4.2.1 Coulomb friction law

Sensitivity tests have been carried out using the Coulomb friction law (Eq. 12), by varying the friction angle δ from 4° to 8°, 1° by 1°, to best fit the observed deposit. The mass reaches the sea position around 60 and 70 s after the initial release of the mass at $t = 0$ s and seems to stop at around 8 min. The best fit of the real deposit runout distance is obtained for a friction angle of about 6° (Fig. 3a, a′). Finer fitting would lead to friction angles slightly larger than 6°. In terms of morphology, the mass spreads laterally, whereas field data exhibit a narrow and elongated shape. The thickness of the modeled deposit reaches more than 90 m down the slope and decreases distally. There is no morphological front and no deposit's tail as well. Note the strong difference in runout distance between $\delta = 6°$ (Fig. 3a, a′) and $\delta = 7°$ (Fig. 2b, b′) (Table 1).

4.2.2 Extended Pouliquen friction law (1999)

Sensitivity tests have been performed using the non-extended and extended Pouliquen friction law (1999), involving two and four friction angles, respectively (Eqs. 14, 15 and 16). The minimum angle δ_1 in Pouliquen friction law (1999) calibrated to reproduce real landslides has been found to be lower than the angle calibrated using a Coulomb friction law (see, e.g., Pirulli and Mangeney 2008). Therefore, we varied δ_1 between 2° and 6° and δ_2 between 12° and 15°, 1° by 1°. We observe the best agreement with the natural deposit for $\delta_1 = 2°$, $\delta_2 = 12°$, $\delta_3 = 4°$ and $\delta_4 = 14°$ (Fig. 3b, b′): the runout distance is well reproduced ($\sim$35 km), and the average thickness is around 10–15 m and a maximum of about 20–25 m. A locally thick sediment packages occur in the center, at the south edge and front of deposit. The latter is 20–25 m high, which is conformed to the reality, and a 15-m-thick deposit's tail also in agreement with observations (Fig. 3b, b′).

4.2.3 Pouliquen and Forterre friction law (2002)

Simulations performed using the Pouliquen and Forterre friction law (2002) with lower friction angles $\delta_1 = 1°$, $\delta_2 = 11°$, $\delta_3 = 3°$ and $\delta_4 = 13°$ display an almost identical deposit, with a quite smaller runout distance $\sim$34.5 km, but longer by 1.5 km compared to the real deposit extent (Fig. 3c, c′). The shape and average thickness are really similar to the previous simulation using the extended Pouliquen friction law (1999) law, both located at the base of the erosive channel and tending to bifurcate toward the south according to the main slope. Only the thickness spatial distribution slightly changes, with a larger and

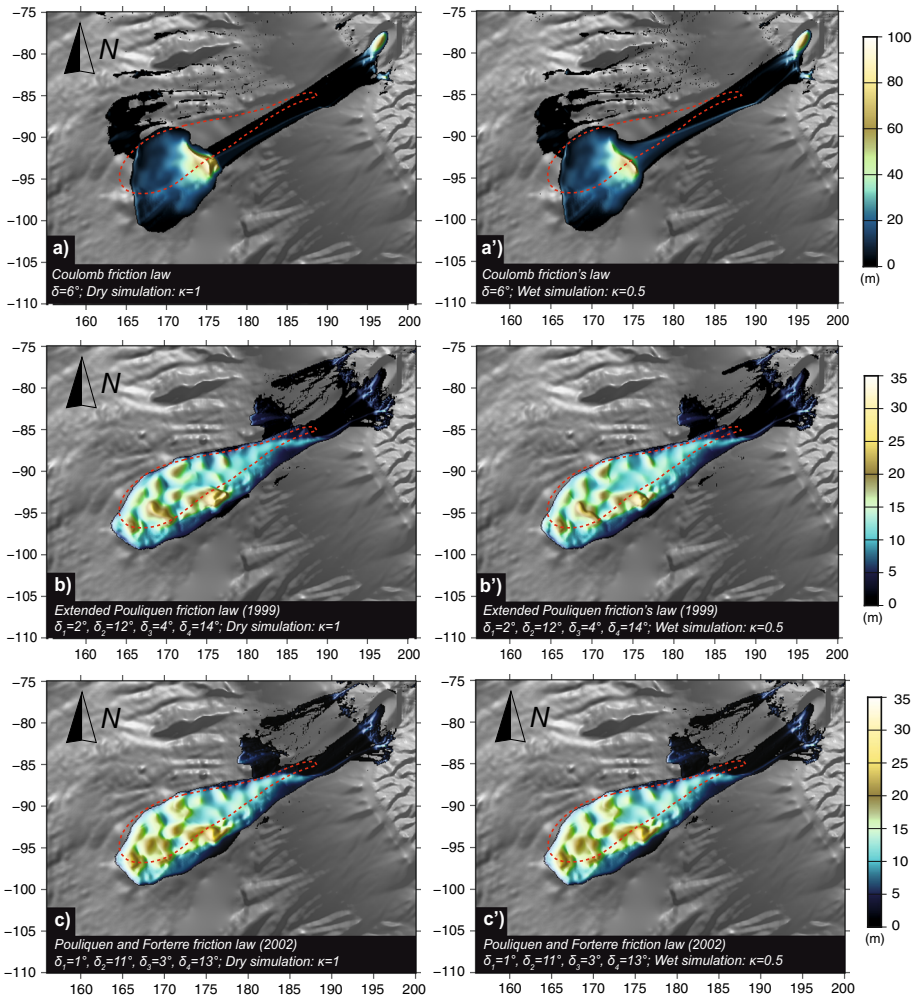

Fig. 3 SHALTOP numerical model: simulations that give the best agreement with observation in terms of runout distance and deposit morphology. Roughness fluctuations have been added to the seafloor in order to consider a more realistic topography. These fluctuations are the same for simulations **a**, **a**′, **b**, **b**′, **c** and **c**′ **a** Coulomb friction law with $\delta_1 = 6°$ and $\kappa = 1$, **a**′ Coulomb friction law with $\delta_1 = 6°$ and $\kappa = 0.5$ **b** extended Pouliquen friction law (1999) with $\delta_1 = 2°$, $\delta_2 = 12°$, $\delta_3 = 4°$, $\delta_4 = 14°$ and $\kappa = 1$, **b**′ extended Pouliquen friction law (1999) with $\delta_1 = 2°$, $\delta_2 = 12°$, $\delta_3 = 4°$, $\delta_4 = 14°$ and $\kappa = 0.5$, **c** Pouliquen and Forterre friction law (2002) with $\delta_1 = 2°$, $\delta_2 = 12°$, $\delta_3 = 4°$, $\delta_4 = 14°$, and $\kappa = 1$, **c**′ Pouliquen and Forterre friction law (2002) with $\delta_1 = 1°$, $\delta_2 = 11°$, $\delta_3 = 3°$, $\delta_4 = 13°$, and $\kappa = 0.5$

thicker central part and a more pronounced front at the snout of the deposit. However, a 10- to 15-m-thick tail is also obtained (Fig. 3c, c′).

Comparing results obtained with the Pouliquen friction law (1999) with two friction angles, and those with the extended Pouliquen friction law (1999) with four friction angles, we notice a greater runout distance for the latter, up to 3 km, and also a width larger by more than 1 km (Figs. 2d, d′, 3b, b′). The modeled deposit with two friction angles is 15–20 m thick in average and up to 30 m in its thickest part. The modeled deposit with

Table 1 Synthesis of best fitted friction angles function of friction laws

Friction law	Coulomb (Le Friant et al. 2003b)	Pouliquen (1999) non-extended (Le Friant et al. 2003b)	Coulomb (this study)	Pouliquen (1999) non-extended (this study)	Pouliquen (1999) extended	Pouliquen (2002)
Best fit friction angles	$\delta_1 = 7°$	$\delta_1 = 6°$ and $\delta_2 = 15°$	$\delta_1 = 6°$	$\delta_1 = 5.5°$ and $\delta_2 = 14.5°$	$\delta_1 = 2°$ $\delta_2 = 12°$ $\delta_3 = 4°$ $\delta_4 = 14°$	$\delta_1 = 1°$ $\delta_2 = 11°$ $\delta_3 = 3°$ $\delta_4 = 13°$

four friction angles is 10–15 m thick in average and up to 25 m thick in its thickest part, with a front forward, which is not observed in the previous case, where a large thickness accumulation occurs slightly backward (Figs. 2c, c′, 3b, b′).

Our results show that the observation does not make it possible to discriminate the different shapes of the friction law (i.e., Pouliquen (1999) or Pouliquen and Forterre (2002)). Indeed, similar deposit can be obtained using these different friction laws but with different friction coefficients. However, the velocity and thickness dependency of the friction law is crucial to reproduce the shape of the deposit as found by Le Friant et al. (2003b) (Table 1). As a result, either of the Pouliquen and co-authors' friction laws with their best fitted friction coefficients can be used to investigate the role of the initial volume and shape of the released mass.

4.2.4 Flow dynamics

To describe the flow dynamics, we thus consider the simulation with the extended Pouliquen law (1999) with friction angles: 2°, 12°, 4° and 14° for dry or wet conditions. Even if simulated deposits appear to be the same in dry or wet simulations, the flow dynamics is expected to change.

For the simulation with dry conditions, once the collapse has started, most part of the slide flows rapidly downslope within the flank collapse structure until the coastline, while a little part is going outside to the north (Fig. 4b). Then, the main mass flow splits into two main units that flow on both sides of a preexisting erosive channel (Fig. 4c). The one that flows against the south wall of the channel rapidly deflects to join the other flow toward southeast (Fig. 4d). Around 20 km off the coastline, the mass thickens and then spreads forward and laterally, conferring a lobate shape to the deposit (Fig. 4e, f). Once it reaches its maximum runout distance, the mass divides in its center into several thick sediment accumulations and a tail is progressively developing backward (Fig. 5g, h). A thicker sediment package is located in front of the deposit, looking like the morphological front observed in the real deposit (Fig. 4h). The simulated flow dynamics helps us to understand the final morphology of the deposit.

Considering wet conditions, we clearly see a difference in terms of dynamics. The first 50 s is pretty corresponding to what we observe in dry conditions, but once the coastline is passed, the mass flow spreads slower (Fig. 4b, b′), so that when the main part of "dry" mass flow has been deflected, the "wet" mass flow is still flowing down along the walls of the channel (Fig. 4c, c′). Despite this time laps between dry and wet simulations, the mass flow evolves exactly the same, by deflecting from the south wall of the channel, starting to get thicker in its center (Fig. 5e, f) before also spreading forward and laterally (Fig. 5g). While the runout distance of the "dry" mass flow was reached at 440 s during the simulation, the "wet" mass flow gets to it at around 600 s (Fig. 5h). This comparison between both dry and wet simulations highlights the first-order influence of water on the flow dynamics, not having an impact on the way the flow propagates, but on the emplacement time (Figs. 4, 5). These different dynamics could not be discriminated by our data on the deposit.

4.3 Sensitivity tests using HYSEA

We use the HYSEA numerical model to assess the effect of the avalanche/water interaction as the debris avalanche is entering the sea and flows down under the water. We used the topography with added roughness.

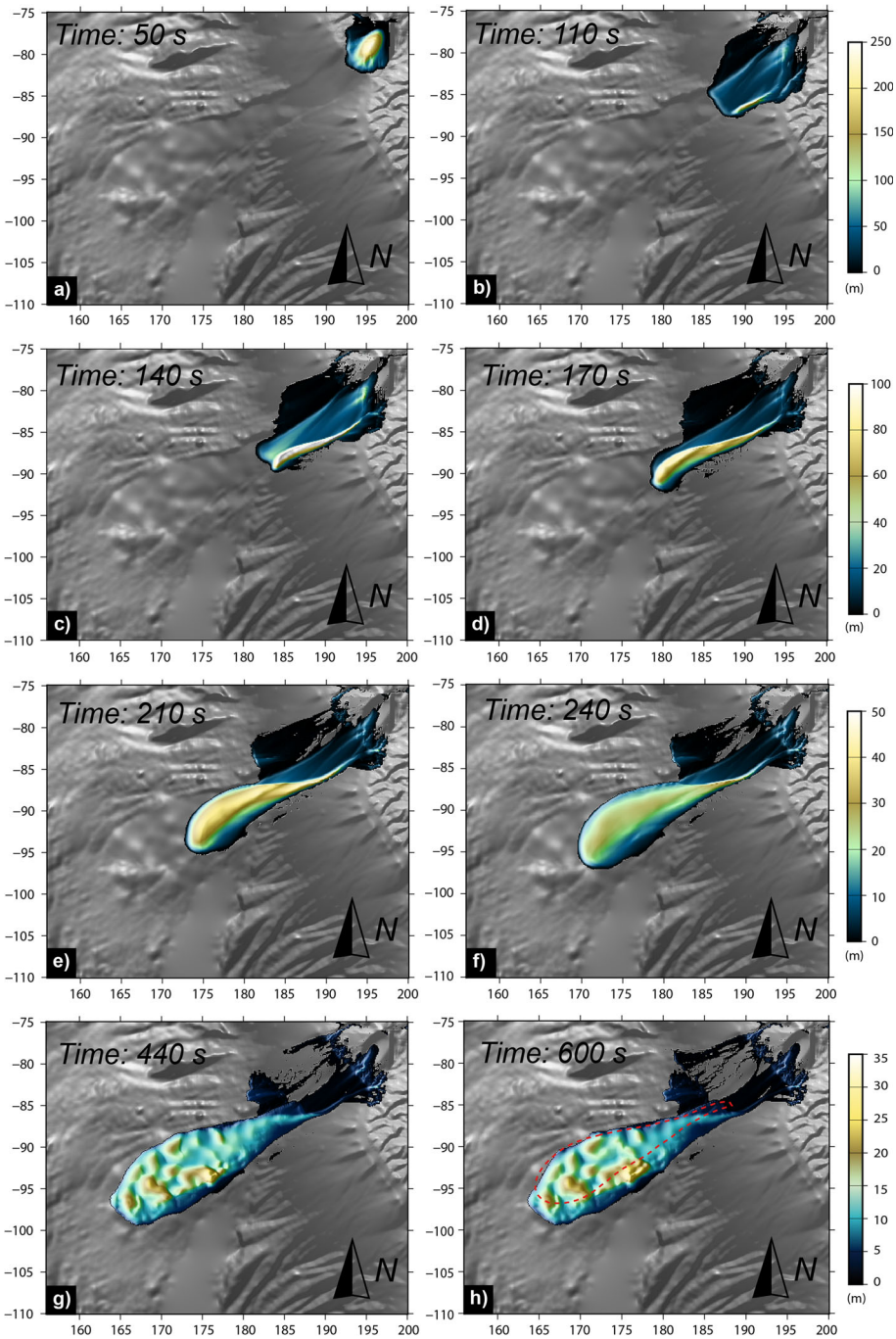

Fig. 4 SHALTOP numerical model: dynamics of the flow in dry conditions ($\kappa = 1$) with the extended Pouliquen friction law (1999) and friction angles $\delta_1 = 2°$, $\delta_2 = 12°$, $\delta_3 = 4°$ and $\delta_4 = 14°$. This is the best agreement in terms of runout distance, morphology of the deposit and thicknesses distribution

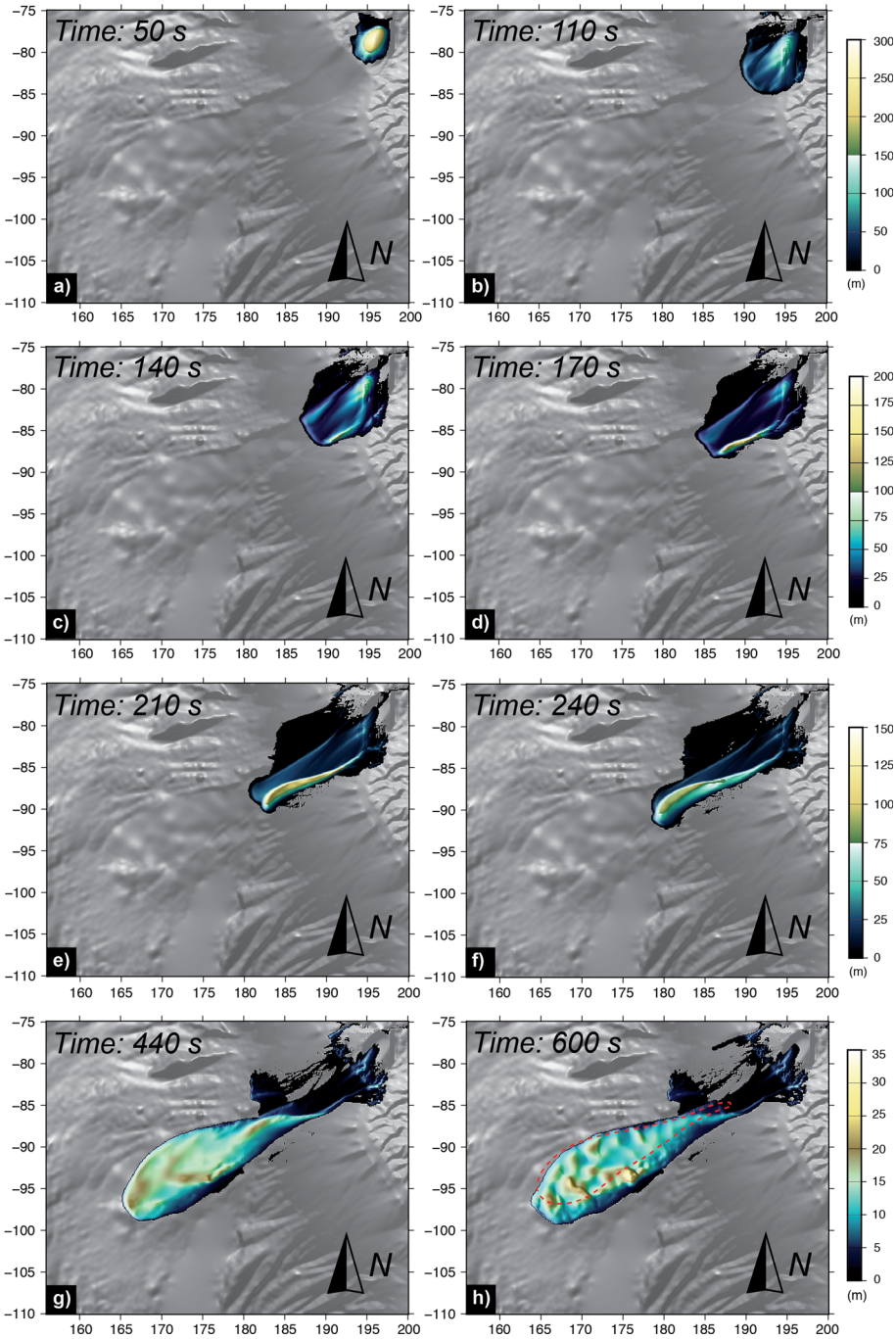

Fig. 5 SHALTOP numerical model: dynamics of the flow in wet conditions ($\kappa = 0.5$) with the Pouliquen friction law (1999) and friction angles $\delta_1 = 2°$, $\delta_2 = 12°$, $\delta_3 = 4°$ and $\delta_4 = 14°$. This is the best agreement in terms of runout distance, morphology of the deposit and thicknesses distribution

Using the same Coulomb friction law and friction coefficient ($\delta_1 = 6°$) as in the simulations with SHALTOP (Fig. 3a, a′), the simulated runout distance is much smaller using HYSEA, in both dry and wet conditions (Fig. 6a, a′). By decreasing the friction angle down to 4°, the "dry" model reaches the real runout (Fig. 6b) but not the "wet" model (Fig. 6b′). The "dry" modeled deposit reaches 30 km off the coast, stuck into the erosive channel, with two zones of thick sediment accumulations, at the foot of the erosive channel and forward in its center part in the deposit (Fig. 6b). The "wet" modeled deposit has a lobate morphology, but is 6 km wider than the observed deposit and is deflected to the

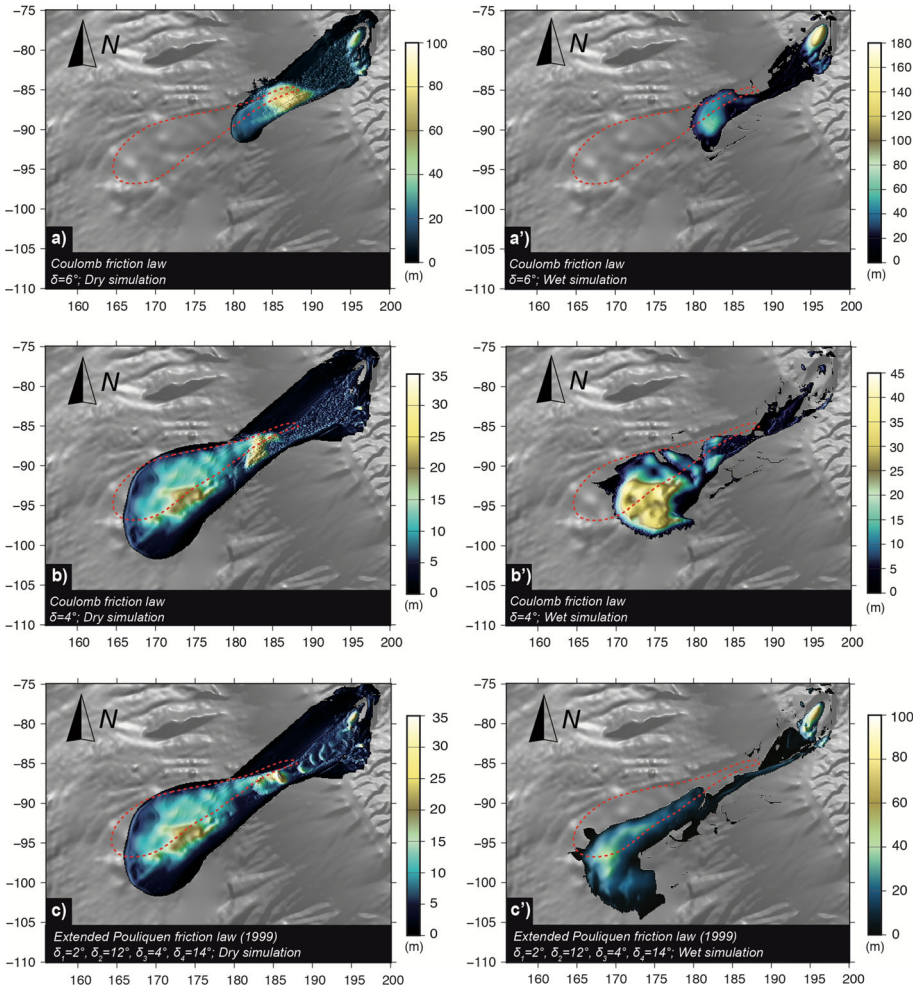

Fig. 6 HYSEA numerical model: sensitivity tests carried out to test the influence of water using the same topography that the one in Fig. 4. **a** Coulomb friction law with $\delta_1 = 6°$ and $\kappa = 1$, **a′** Coulomb friction law with $\delta_1 = 6°$ and $\kappa = 0.5$, **b** Coulomb friction law with $\delta_1 = 4°$ and $\kappa = 1$, **b′** Coulomb friction law with $\delta_1 = 4°$ and $\kappa = 0.5$, **c** extended Pouliquen friction law (1999) with $\delta_1 = 2°$, $\delta_2 = 12°$, $\delta_3 = 4°$, $\delta_4 = 14°$ and $\kappa = 1$, **c′** extended Pouliquen friction law (1999) with $\delta_1 = 2°$, $\delta_2 = 12°$, $\delta_3 = 4°$, $\delta_4 = 14°$ and $\kappa = 0.5$. Simulations performed with the Coulomb friction law, demonstrating that it is necessary to consider smaller friction angles to obtain approximately runout distance equivalent to that obtained with the SHALTOP numerical model

Fig. 7 HYSEA numerical model: dynamics of the flow in wet conditions with the extended Pouliquen friction law (1999), and friction angles $\delta_1 = 2°$, $\delta_2 = 12°$, $\delta_3 = 4°$ and $\delta_4 = 14°$. The runout distance is well reproduced but not of the morphology and thickness distribution of the deposit. The avalanche dynamics is also very different compared to the one simulated by the SHALTOP numerical model (Figs. 4, 5)

south. Most of the mass flow sediments concentrate forward, forming a large front (Fig. 6b′). We observe no tail at the rear of the slide (Fig. 6b′). Therefore, using a Coulomb friction law under dry conditions, the HYSEA model well reproduces the deposit in terms of morphology. We can see here that, with the Coulomb friction law, the errors in the topography description in HYSEA artificially lead to a better fit with the observed deposit than when using the SHALTOP model.

Simulation with HYSEA using the extended Pouliquen friction law (1999) with the same parameters as in SHALTOP ($\delta_1 = 2°$, $\delta_2 = 12°$, $\delta_3 = 4°$ and $\delta_4 = 14°$) shows similar morphology and thickness distribution than those obtained with the Coulomb friction law ($\delta = 4°$) in dry conditions (Fig. 6b, c). However, considering wet conditions, the results are different. Indeed, although the runout distance is similar to previous simulations and in line with the observed deposit, the shape of the modeled deposit is very different. It shows a "L" shape elongated until the runout distance with sediment accumulation at this point, and some thinner part to the south (Fig. 6c′). A central mass and elongated from north to south is located at the front of the deposit, and then two arms extend northwest (forming a tail at the rear of the deposit) and south (Fig. 6c′).

Using the HYSEA, there is globally a better fit with the real DAD3 deposit when considering dry rather than wet conditions. However, both drift southward contrary to the real deposit. Moreover, the sediment distribution is not well reproduced in both simulations.

Comparison between Figs. 4, 5 and 7 shows that the flow dynamics is really different using the HYSEA numerical model compared to SHALTOP even though both were carried out with the same parameters (roughness, extended Pouliquen law (1999), with friction angles $\delta_1 = 2°$, $\delta_2 = 12°$, $\delta_3 = 4°$ and $\delta_4 = 14°$, wet conditions). With HYSEA, once the collapse has started, most part of the avalanche rapidly reaches the coastline, with really little material going outside of the flank collapse structure (Fig. 7a). Then, as observed with SHALTOP, the mass splits into two main units that flow on both sides of the submarine channel (Fig. 7b). Although at this stage, the runout distance of the avalanche is lower by 5 km than the one calculated with SHALTOP (Fig. 4c), most of the avalanche is also concentrated at the south wall of the channel (Fig. 7c). Contrary to the avalanche modeled in dry conditions, here it continues to flow along the channel's wall (Fig. 7d) and progressively spreads longitudinally with no such obliquity on the north side of the flow, as observed in the dry simulation (Figs. 4e, 7e). Moreover, at this stage, the runout distance is much smaller than in the SHALTOP's dry simulation, of about 10 km. Then, the avalanche continues to flow straight ahead and starts slightly to bifurcate southward (Fig. 7f). Then, the avalanche continues to evolve in both directions (Fig. 7g) and finally stops around 30 km off the coast as the modeled deposit in the SHALTOP's dry simulation (Figs. 7h, 4h). The shape of the deposit is totally different from the real one and from the one modeled with the SHALTOP dry simulation (Figs. 2a, 7h).

Using the HYSEA numerical model but considering this time dry conditions (Fig. 8), we clearly see a similar flow dynamic as observed with SHALTOP (Fig. 4), except that a large part of the mass flow gets northward of the flank collapse structure since the beginning of the simulation (Fig. 8a, b). The avalanche also seems to flow down

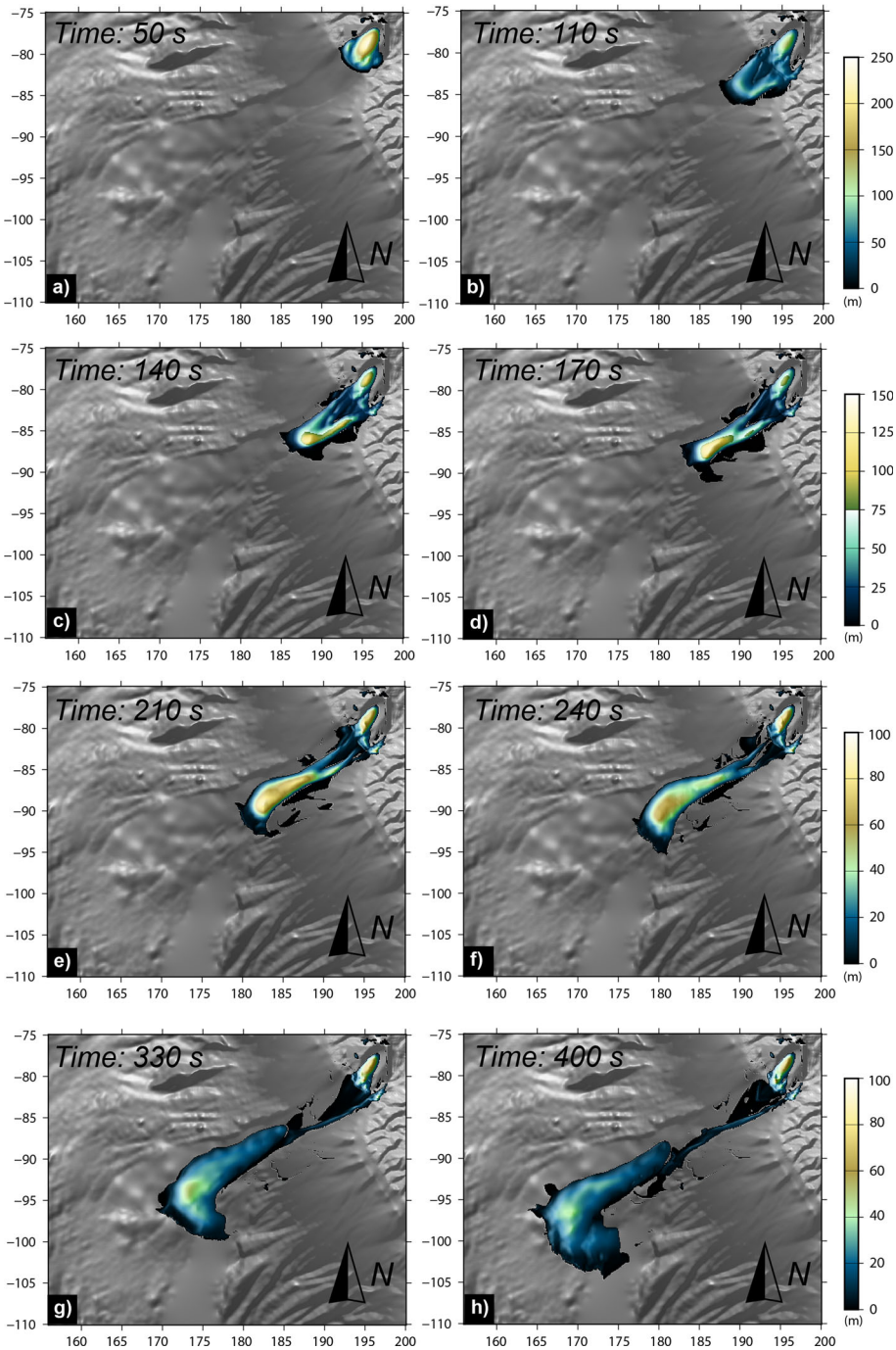
Time: 50 s
a)
Time: 110 s
b)
Time: 140 s
c)
Time: 170 s
d)
Time: 210 s
e)
Time: 240 s
f)
Time: 330 s
g)
Time: 400 s
h)
N
(m)

Fig. 8 HYSEA numerical model: dynamics of the flow in dry conditions with the extended Pouliquen friction law (1999) and friction angles $\delta_1 = 2°$, $\delta_2 = 12°$, $\delta_3 = 4°$ and $\delta_4 = 14°$. The runout distance is well reproduced, but not the final deposit that is located too far southward compared to the real one. Scattered sediment accumulation is also not reproduced. However, the avalanche dynamics is close to the one simulated by the SHALTOP numerical model (Figs. 4 and 5)

preferentially along the south wall of the channel (Fig. 8c, d), before drifting westward (Fig. 8e, f) and spreading forward and laterally (Fig. 8g, h). Compared to the dry simulation with SHALTOP (Fig. 4) the runout distance during the avalanche's emplacement is systematically lower, but the final runout distance is the same. However, the thickness distribution within the deposit is different, with one main sediment accumulation in the center of the deposit (Fig. 8h). Compared to the wet simulation with HYSEA (Fig. 7), there is no such difference in terms of runout distance during the avalanche's emplacement. However, as described before, the dynamic emplacement is very different and the final outline deposit as well (Figs. 7, 8). We also notice that the avalanche is directly channeled into the erosive channel when it enters the sea in the wet simulation (Fig. 7b) while it is more widespread in the dry simulation (Fig. 8b).

5 Discussion

5.1 Interactions between the avalanche and water: SHALTOP versus HYSEA

While SHALTOP gives the same deposits for wet and dry simulations, HYSEA that accounts for the interaction between the submarine avalanche and the water column predicts different deposits for wet and dry simulations, as shown in Eqs. (8). For the same Coulomb friction law, simulations using HYSEA required lower friction angles (2° to 3°) to obtain the same runout distance than simulations using SHALTOP. For the value of friction angles ($\delta_1 = 6°$), the difference in runout distance is about 16 km between the two models (Figs. 3a, a′, 6a, a′) and about 1–2 km using the extended Pouliquen friction law (1999) (Figs. 3b, b′, 6c, c′). It is hard to discriminate between the effect of water and the impact of the difference in the description of the topography when comparing the two models.

Whatever, in terms of combined runout distances, shape, morphology and material distribution, the calculated deposit simulated with SHALTOP better fits the real deposit using both the extended Pouliquen friction law (1999) and the Pouliquen and Forterre friction law (2002) (Fig. 3b, b′, c, c′). Indeed, there are no such differences between both simulated deposits, as testified by the calculation of the runout error and the misfit. The latter represents the mean difference between the observed and the simulated deposit, in terms of height (Table 2; Fig. 9).

$$\text{misfit} = \sqrt{\frac{1}{N}\sum_i \sum_j \left(h_M(i,j) - h_S(i,j)\right)^2} \tag{22}$$

where h_M is the measured height, h_S is the simulated height, and i and j are the indexes of the topography grid.

On contrary, simulations using the HYSEA model display substantial differences with the real deposit (Fig. 6c, c′). To better understand the effect of the different terms in the HYSEA model, we varied the friction between the fluid and the avalanche layers for both

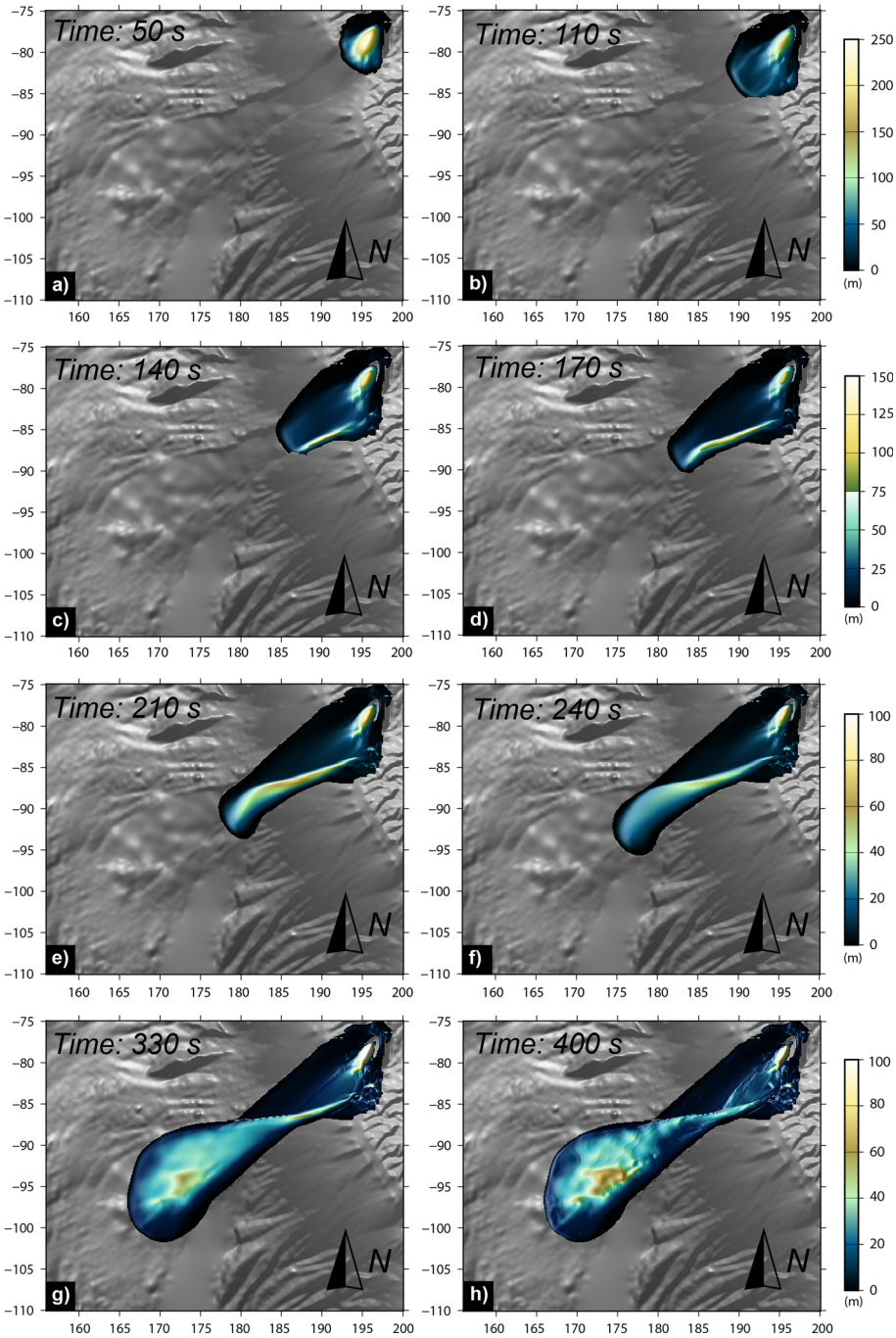

Coulomb and Pouliquen friction laws. We found that this friction term only slightly changed the avalanche dynamics and deposit while it changes the tsunami waves generated by the avalanche. The main difference between the dry and wet simulations in HYSEA is

Table 2 Synthesis of the deposit height misfit and the runout relative error between the modeled and real deposits

Best fit with friction laws	Height misfit (m)	Runout relative error (%)
Coulomb: $\delta = 6°$	17.7	5.5
Pouliquen and Forterre friction law (2002): $\delta_1 = 1°$; $\delta_2 = 11°$; $\delta_3 = 3°$; $\delta_4 = 13°$	10.7	3.8
Extended Pouliquen friction law (1999): $\delta_1 = 2°$; $\delta_2 = 12°$; $\delta_3 = 4°$; $\delta_4 = 13°$	10.6	3.8
Pouliquen friction law (1999): $\delta_1 = 5.5°$; $\delta_2 = 14.5°$	12.4	3.4

The runout error is calculated as follows: $\frac{|r_M - r_S|}{r_S}$ where r_M and r_S are the measured and simulated runout distances. Simulations presented here were carried out with the SHALTOP numerical model

related to the entry of the avalanche into the water. Indeed, at that moment the gravity sharply changes from g to the reduced gravity, generating a sharp change in the velocity field. This change and the presence of complex eigenvalues in the two-layer model are hard to deal with numerically (Fernandez-Nieto et al. 2008). Furthermore, the entry of the avalanche into the water involves complex 3D motion that could not be properly handled by thin-layer depth-averaged models. Another key point that is not taken into account in HYSEA is the dilatancy effects that generate a coupling between the granular phase and the pore fluid pressure that can drastically change the flow dynamics and deposit (Rondon et al. 2011; Bouchut et al. 2016). Detailed comparison with laboratory experiments should be done to get better insights into the validity and limits of two-layer depth-averaged model to simulate granular flows entering water (e.g., Viroulet et al. 2014).

Furthermore, as discussed in introduction, the description of topography effects in HYSEA is not accurate [thin-layer approximation applied in the horizontal/vertical reference frame in Fernandez-Nieto et al. (2008)]. On the other hand, SHALTOP properly takes into account the thin-layer approximation in the direction normal to the topography and involves the full tensor of the topography curvature contrary to the HYSEA numerical model that only use part of the curvature terms thus neglecting some centrifugal forces. These forces may, however, play a key role in the avalanche dynamics (Favreau et al. 2010; Moretti et al. 2015).

For these reasons, we will therefore use SHALTOP to simulate different debris avalanches offshore Martinique to assess the effect of the released volume on the runout distance (Sect. 4.2).

5.2 Low friction angle and influence of the flow parameters

The DAD3 deposit is well modeled with the extended Pouliquen friction law (1999), suggesting a dependence of the empirical friction coefficient on the thickness and velocity of the flowing mass. This is in agreement with the conclusions of Le Friant et al. (2003b). Other approaches based on simulations of a wide range of landslides on Earth and other planets showed that the empirical friction coefficient decreases with the volume involved V (Lucas et al. 2014):

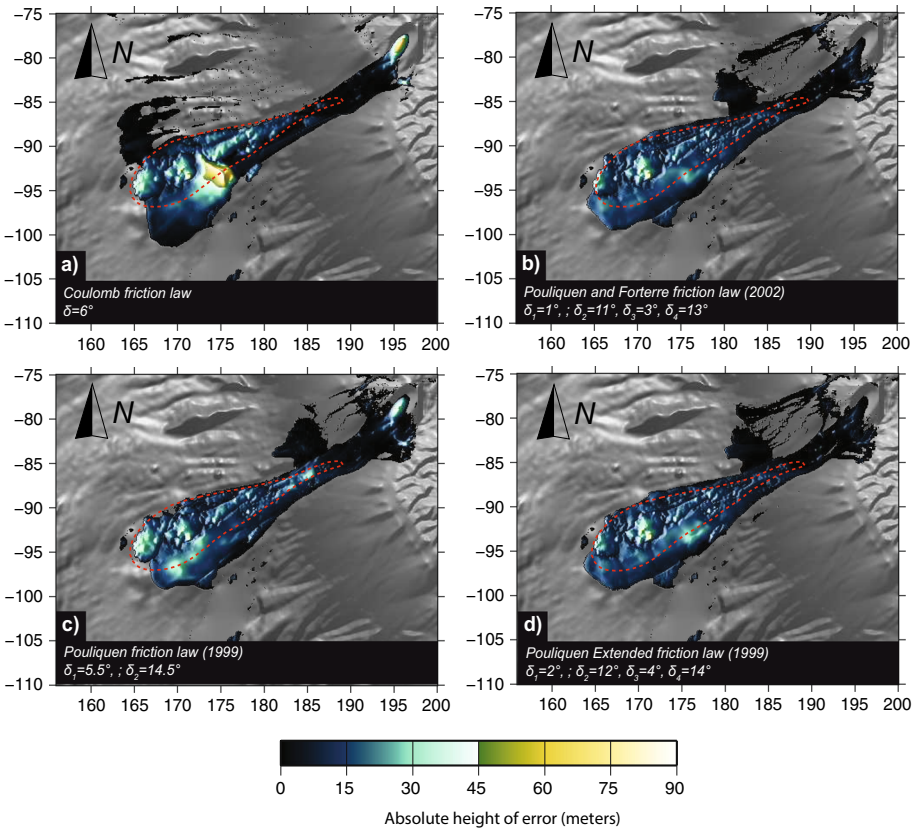

Fig. 9 Illustration of the absolute height errors for the best fitted simulations using the SHALTOP numerical model, in relation to the real deposit: **a** Coulomb friction law with $\delta_1 = 6°$, **b** Pouliquen and Forterre friction law (2002) with $\delta_1 = 1°$, $\delta_2 = 11°$, $\delta_3 = 3°$, $\delta_4 = 13°$, **c** non-extended Pouliquen friction law (1999) with $\delta_1 = 5.5°$, $\delta_2 = 14.5°$ and **d** extended Pouliquen friction law (1999) with $\delta_1 = 2°$, $\delta_2 = 12°$, $\delta_3 = 4°$, $\delta_4 = 14°$

$$\mu_{\text{eff}} \sim V^{-0.0774} \tag{23}$$

As the landslide velocity is related to the volume, the friction coefficient could also be expressed empirically as a function of velocity (Lucas et al. 2014). Using Eq. (2) for the large-scale volume 1.8×10^9 m^3 DAD3 deposit leads to a small friction coefficient $\mu_{\text{eff}} \sim 0.192$ as shown in Fig. 10a. This represents a friction angle of 10.8°. The best fitted friction angle obtained with the Coulomb friction law $\delta = 6°$ is much smaller, corresponding to $\mu_{\text{eff}} \sim 0.105$ (see Fig. 10a). Because Eq. (23) has been obtained using the best fitted friction coefficients of the Coulomb friction law, this may suggest that a lower friction coefficient needs to be used to simulate submarine avalanches compared to dry avalanches.

However, the value of $\mu_{\text{eff}} \sim 0.192$ deduced from (24) well corresponds to the range of friction angles used for the simulation with the extended Pouliquen friction law (1999) that best reproduces the observed deposit (Fig. 3b, b′). This is demonstrated in Fig. 11, where the friction angle from this simulation is represented. It varies between 10.5° and 11°

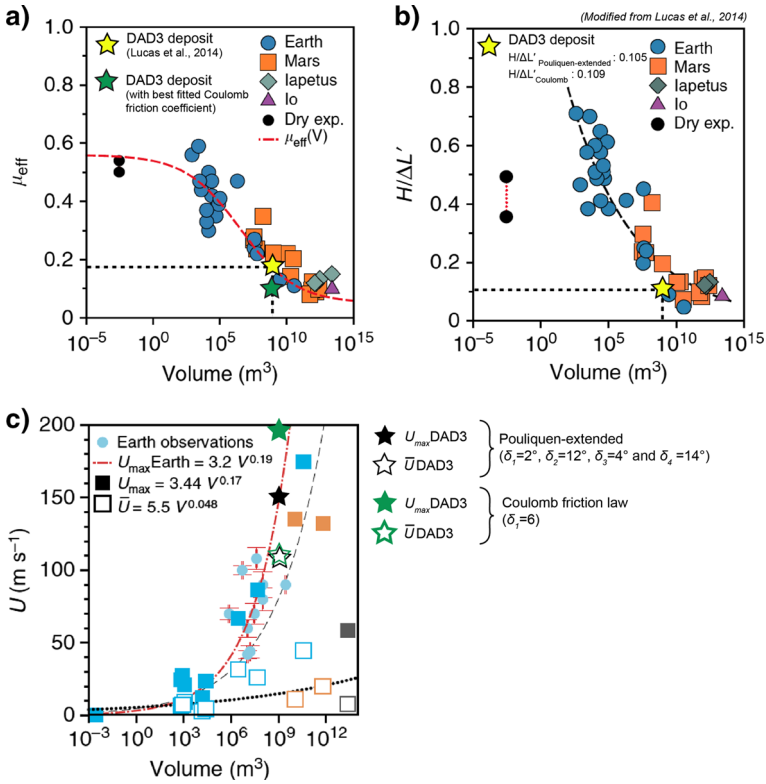

Fig. 10 Characterization of DAD3 deposit (*yellow* and *green stars*) in terms of **a** effective friction (see Lucas et al. 2014 for more details), **b** Heim's ratio and **c** velocities as a function of volume (figures are modified from Lucas et al. 2014)

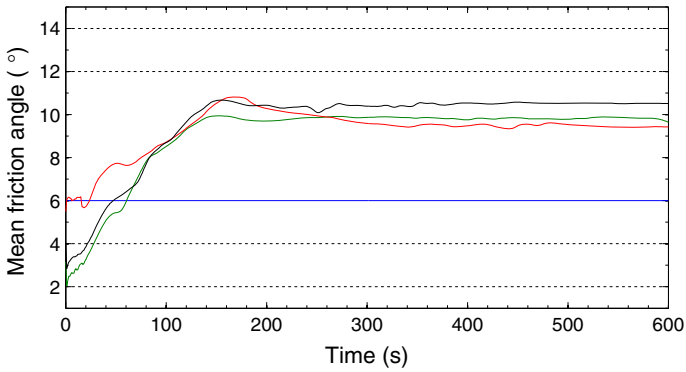

Fig. 11 Evolution of the mean friction angle during the SHALTOP simulations that best reproduces the observed deposit (i.e., Coulomb friction law with $\delta_1 = 6°$ in *blue*, the non-extended Pouliquen friction law with two angles $\delta_1 = 5.5°$, $\delta_2 = 14.5°$ in *red*, the extended Pouliquen friction law (1999) with four angles: $\delta_1 = 2°$, $\delta_2 = 12°$, $\delta_3 = 4°$, $\delta_4 = 14°$ in *black* and the Pouliquen friction law (2002) with four angles $\delta_1 = 1°$, $\delta_2 = 11°$, $\delta_3 = 3°$, $\delta_4 = 13°$ in *green*). After the first 150 s, friction angle stays quite stable around 9° and 11°

during a large part of the avalanche's emplacement. Interestingly, the value of the mean friction coefficient used here for a submarine debris avalanche is close to that obtained for subaerial avalanches of the same volume. The use of more complex friction law than the Coulomb friction law could possibly help to get better empirical relations than (19). Note that the corresponding Heim's ratio is also very small (Fig. 10b).

Considering the volume of the DAD3 deposit (1.8 km^3) in the empirical figures obtained by Lucas et al. (2014) from simulations of a wide range of landslides leads to a maximum velocity of the avalanche of 150 m/s and 200 m/s depending on the friction law (Fig. 10c) and mean velocity between 110 and 112 m/s.

As commonly described in the literature, for large landslides, the debris avalanche deposit mobility and deposition processes are well reproduced with a low empirical value of the friction coefficient (Lucas et al. 2014). The corresponding empirical friction angles are much smaller than the static friction angles of volcanic rocks and sediments and than the angles required in numerical models to reproduce laboratory experiments (e.g., Mangeney-Castelnau et al. 2005; Ionescu et al. 2015). The origin of this low friction is still an open issue even though it is commonly explained by the fact that pore pressure is not explicitly taken into account in the models (Voight et al. 2002 and Kelfoun and Vargas 2015) or by the development of a boundary layer at the base of the debris avalanche (e.g., Campbell et al. 1995). Others studies based on field data also proposed and quantified a statistical relation between a volume and the effective friction (i.e., ratio of the fall height to the runout distance) (Legros 2002; Bayarri et al. 2015). Even if authors observed a strong negative correlation between the effective friction and the volume, they proposed that increase in runout distance due to a large volume corresponds to a decrease in the effective friction, so that larger flows generate lower effective dissipation. Legros (2002) goes further, suggesting that in some cases, the runout of a landslide passing a certain distance would depend on the volume beyond this distance and not on the total volume of the landslide. Some well-documented examples of landslides and notably debris avalanches from flank collapse events at Mount Shasta or Mount St. Helens—like those affecting Montagne Pelée volcano—were in agreement with this theory. This prediction notably suggests that landslides hazards assessment should be based on the correlation between the volume and the area covered by the deposit, rather than on the effective friction.

5.3 Influence of the avalanche volume on deposit extent

The good agreement between our simulations with SHALTOP and the observed deposit, as well as the similitude of the friction coefficients used here and those calibrated for other events (Lucas et al. 2014), suggests that this model and friction parameters could be used to investigate the dynamics and deposit of debris avalanches in this area. In particular, our results reinforce the suggestion that the debris avalanche's extent is influenced by the transition between submarine volcano flank and Grenada Basin as suggested by the interpretation of Brunet et al. (2016). However, bigger volumes of the old events are not fully constrained so that some questions remain, such as: could debris avalanches with bigger volumes travel much further? Do these events occur in one time or in several phases? To investigate this, simulations were carried out by testing different initial collapse volumes varying from 0.5 up to 7 km^3. We varied the height H_0 of the initial masses between 90 and 580 m and the width W_0 between 1 and 15 km. This range of volumes has been simulated to take into account bigger volumes that may have collapsed in the past in the Montagne Pelée volcano history, as represented in Fig. 12.

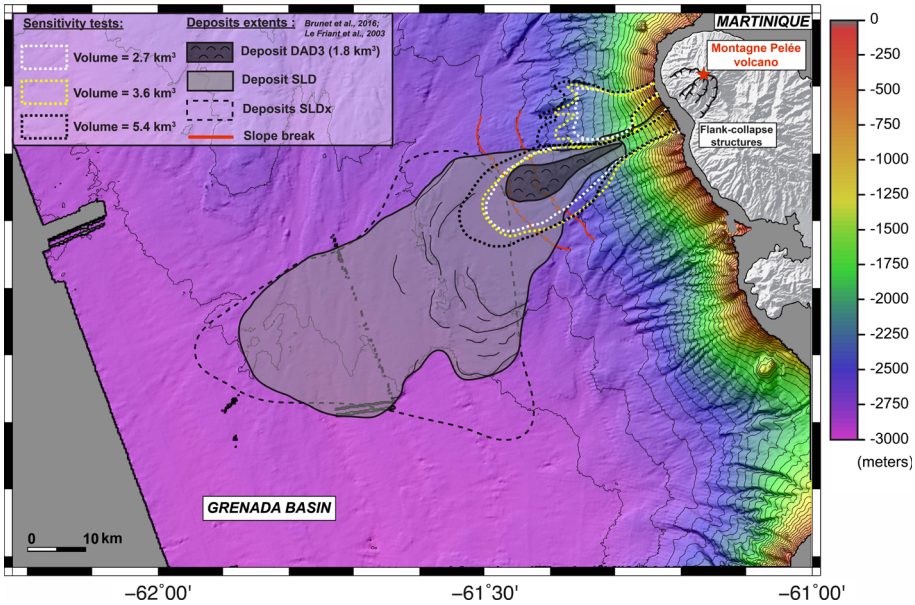

Fig. 12 Sensitivity tests performed to test the influence of the collapse volume by varying its height. Simulations are systematically carried out using the extended Pouliquen friction law (1999) with $\delta_1 = 2°$, $\delta_2 = 12°$, $\delta_3 = 4°$, $\delta_4 = 14°$ and $\kappa = 1$. **a** Initial collapse volume = 1.8 km^3, **b** initial collapse volume = 2.7 km^3, **c** initial collapse volume = 3.6 km^3 and **d** initial collapse volume = 5.4 km^3. Simulation time has been extended for simulations considering more than twice the real volume (**c**, **d**). **e** Bathymetric map representing the extents of calculated deposits using different volumes of debris avalanche collapses. The corresponding runout distances vary only slightly

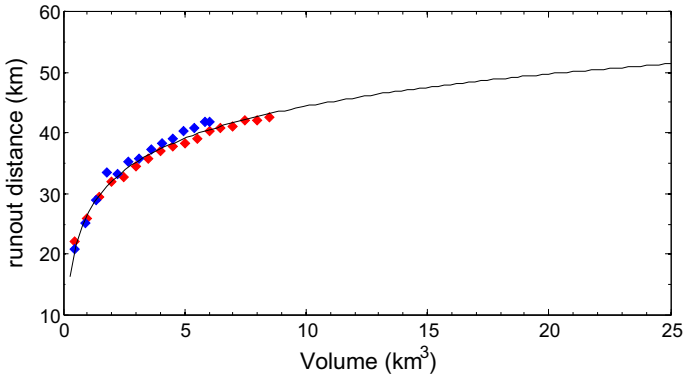

Fig. 13 Illustration of the runout distance as a function of the volume of the released mass. The *blue diamonds* represent simulations with variable height and fixed width of the collapse dome, while the *red diamonds* correspond to simulations with variable width and fixed height. Both demonstrate the increase in runout distance with increasing debris avalanche volumes, and especially a slower growth around 30–35 km from the coastline. The latter corresponds to the transition between the submarine volcano flank and the Grenada Basin

Since the sliding mass is greater, the runout distance is longer (Fig. 13). However, depending on the chosen variable parameter (height versus width of the collapse dome), the debris avalanche's runout distance is slightly different. Indeed, for the same volume, simulations with a variable width systematically show lower runout distance compared to those with a variable height (Fig. 13). For instance, considering a collapse material of 6 km^3, the runout distance is around 42 km for simulations with $H_0 = 565$ m and $W_0 = 510$ m and 40 km for simulations with $W_0 = 1230$ m $H_0 = 100$ m (Fig. 13). However, the runout distance growth with the debris avalanche volume is clearly increasing less when the avalanche reaches distances of about 30–35 km from the coastline, either considering height or width variations (Fig. 13).

In addition, the increase in runout distance displays two phases: a significant increase in the runout as a function of the volume involved until 35 km offshore the coastline for debris avalanches up to 3 km^3, and a slower but continuous increase in runout as a function of the volume involved for bigger debris avalanches (Fig. 13). This specific distance corresponds to the transition between the submarine volcano flank and the Grenada Basin (between 2° and 0.5°). Indeed, this break in slope tends to slow down the debris avalanches propagation and may act as an accumulation zone for debris avalanche deposits of volumes around 2–5 km^3 (Figs. 12, 13). In addition, numerical simulations modeling four successive flows (5 km^3 each; Fig. 14a–d) and resulting deposits thickness accumulation (Fig. 14e) support this assumption. Each simulation takes into account the new topography resulting from the emplacement of a previous deposit. For instance, modeling of the 2nd flow (Fig. 14b) has been undertaken considering the new topography resulting from the 1st flow modeling (Fig. 14a), and so on. Then, simulations show that runout distance is not increasing with the number of flows deposits, but stays stable around 35–40 km offshore the island. Plus, deposits still display an accumulation zone at the front (20–30 m thick), a lobate shape and a deposit tail (10 m thick). Figure 14e shows that north to the main deposit unit, there is another smaller accumulation zone, still located at the transition between the submarine volcano flank and the Grenada Basin (around 2500 m deep). Thus, the runout distance appears to be here mainly related to the seafloor's configuration that is strongly supporting our assumption.

Considering larger debris avalanche volumes, the runout distance still slightly increases, so that debris avalanches as big as 25 km^3 may reach 50 km from the coastline (Fig. 13). Previous studies have estimated such collapse volumes based on older and larger flank collapse structures on-land (Deplus et al. 2001; Le Friant et al. 2003a; Boudon et al. 2007). However, drilled cores from IODP 340 expedition have demonstrated that no debris avalanche deposits coming from the volcano can be identified 50 km offshore the island. Debris avalanche deposits have been only identified around 33 km offshore, at 1401 drill sites (Le Friant et al. 2015; Brunet et al. 2016). Moreover, our numerical simulations suggest that previous larger flank collapses probably occurred in several times with successive debris avalanches volumes ($\sim$2–5 km^3) entering the sea and traveling distances no more than 40 km (Fig. 14). More detailed shapes and position of the released mass of these high volumes events should be performed to confirm our results. However, we expect to obtain similar results on the dependence of the runout distance on the volume because changing the height or the width of the released mass gives approximately the same tendency (Fig. 13).

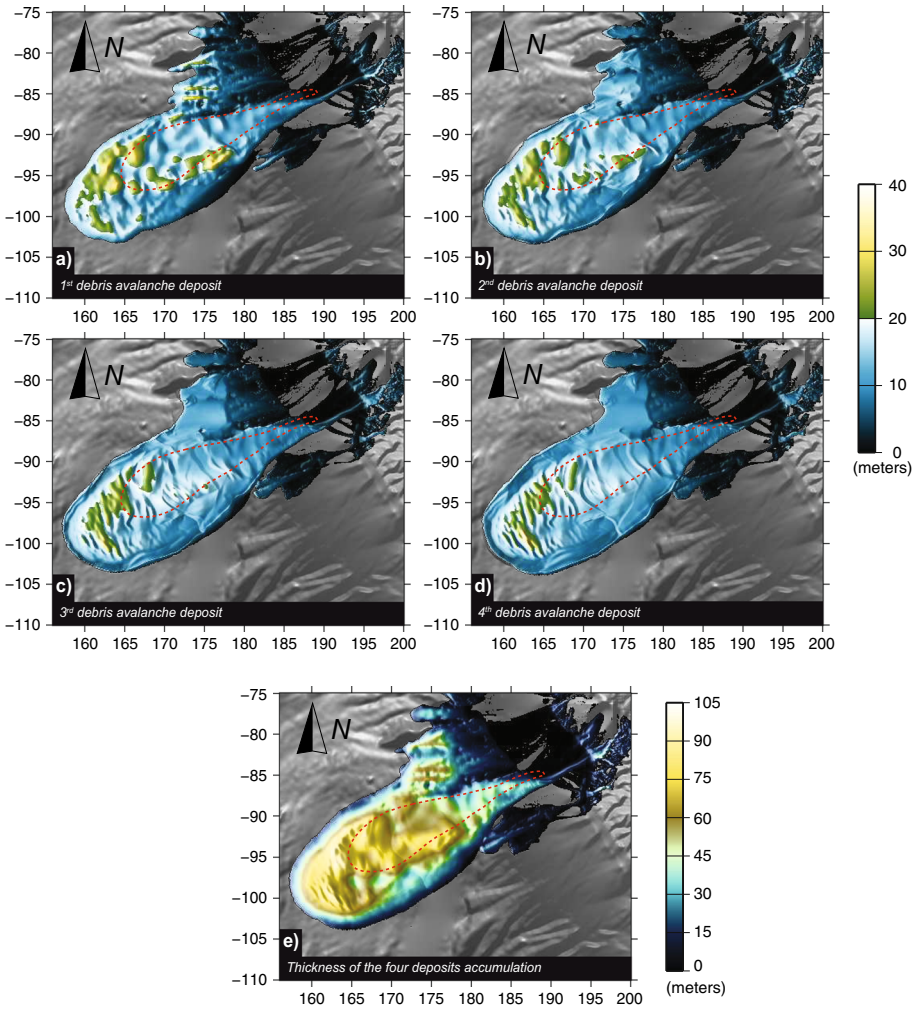

Fig. 14 Simulation carried out with the SHALTOP numerical model representing (**a**, **b**, **c** and **d**) four successive debris avalanche deposits (5 km^3 each) and **e** resulting thickness accumulation. The runout distance is not increasing with the number of flows deposits, but stays stable around 35–40 km offshore the island

6 Conclusion

The DAD3 debris avalanche deposit related to the last Montagne Pelée flank collapse is better reproduced with the SHALTOP model than with the HYSEA model. This suggests that (i) the accurate description of the topography is a crucial ingredient in the dynamics and deposition of such debris avalanches and (ii) the theoretical and numerical description of the entering of the debris avalanche into the water has to be more accurately simulated than what is presently done in HYSEA. In particular, 3D effects or dilatation/compression effects and their interaction with pore fluid pressure that are ignored in state-of-the-art thin-

layer depth-averaged models may play a strong role in the dynamics and deposit of aerial avalanches entering the sea.

The best agreement with observations is obtained using the Pouliquen and co-authors friction laws and, for example, for the extended Pouliquen (1999) with friction angles $\delta_1 = 2°$, $\delta_2 = 12°$, $\delta_3 = 4°$ and $\delta_4 = 14°$. Sensitivity tests using different topographies and mass volumes show a debris avalanches critical runout distance around 30–40 km offshore the island, corresponding to the transition between the submarine volcano flank and Grenada Basin, for avalanches with volumes of about 2–5 km^3. If compared to simulations, the use of seismic signals generated by the flow that are recorded for more recent avalanches would have helped to constrain the different dynamical scenario and time variations of the force applied by the landslide to the topography, providing new types of data that will possibly help going further in investigating this issue (see, e.g., Favreau et al. 2010; Schneider et al. 2010; Hibert et al. 2011; Moretti et al. 2012, 2015; Levy et al. 2015; Yamada et al. 2016). However, this latter approach does not allow to constrain the dynamics of past events, like the one studied here.

Simulations show that the more voluminous debris avalanches from Montagne Pelée's collapse events proposed in the literature ($V \sim 25$ km^3) may extend until 50 km offshore, with changing either the height or the width of the released mass (Fig. 13). Moreover, our simulations demonstrate that runout distance is not increasing with successive flows of volumes smaller than about 5 km^3 and stays around 35–40 km offshore the island. These observations associated with field data showing that debris avalanche deposits could only be found up to 35 km offshore the island, suggest that volcano flank collapse might occur in several phases involving debris avalanches volumes no more than 5 km^3 and therefore smaller runout distances than previously thought. These multistage volcano flank collapses are a common process in the Lesser Antilles, especially in Montserrat Island (e.g., Cassidy et al. 2012) but has been also described in others volcanic islands contexts. For instance, the Canary and Hawaiian Islands have generated distinctive turbidites that comprise multiple fining-upward subunits (Garcia and Meyerhoff Hull 1994; Wynn and Masson 2003; Hunt et al. 2011, 2013), which suggest that flank collapse occurred in a number of stages separated by days to weeks. Therefore, our study highlights the necessity to focus on the timing of emplacement process of the previous volcano flank collapse events, which is crucial to well evaluate the resulting tsunamigenic hazard in Martinique, but also in the Lesser Antilles arc, which is largely prone to these processes.

Acknowledgements We thank Christine Deplus and staff scientists for the data provided by the AGUADOMAR and CARAVAL cruises. IGN provided to IPGP volcano observatories the DTM of Martinique Island used in this study. This study was financially supported by the ANR-13-BS06-0009 CARIB and the Labex UnivEarthS. For the numerical aspects, this work has been funded by the ANR contract ANR-11-BS01-0016 LANDQUAKES, the USPC PEGES project and the ERC contract ERC-CG-2013-PE10-617472 SLIDEQUAKES and the Spanish Government and FEDER through the Research Project MTM2015-70490-C2-2-R.

References

Abadie S, Morichon D, Grilli S, Glockner S (2008) VOF/Navier-Stokes numerical modeling of surface waves generated by subaerial landslides. La Houille Blanche 1:21–26. doi:10.1051/lhb:2008001

Abadie S, Morichon D, Grilli S, Glockner S (2010) Numerical simulation of waves generated by landslide using a multiple-fluid Navier–Stokes model. Coast Eng 57:779–794. doi:10.1016/j.coastaleng.2010.03.003

Abadie S, Harris J, Grilli S (2011, January) Numerical simulation of tsunami generation by the potential flank collapse of the Cumbre Vieja Volcano. In: The 21st international offshore and polar engineering conference. International Society of Offshore and Polar Engineers

Abadie SM, Harris JC, Grilli ST, Fabre R (2012) Numerical modeling of tsunami waves generated by the flank collapse of the Cumbre Vieja Volcano (La Palma, Canary Islands): tsunami source and near field effects. J Geophys Res Oceans 117(C5):C05030

Bayarri MJ, Berger JO, Calder ES, Patra AK, Pitman EB, Spiller ET, Wolpert RL (2015) Probabilistic quantification of hazards: a methodology using small ensembles of physics-based simulations and statistical surrogates. Int J Uncertain Quantif 5(4):297–325

Bouchut F, Westdickenberg M (2004) Gravity driven shallow water models for arbitrary topography. Commun Math Sci 2(3):359–389

Bouchut F, Mangeney-Castelnau A, Perthame B, Vilotte J-P (2003) A new model of saint venant and savage-hutter type for gravity driven shallow water flows. CR Math 336(6):531–536

Bouchut F, Fernandez-Nieto ED, Mangeney A, Narbona-Reina G (2015a) A two-phase shallow debris flow model with energy balance. Math Model Num Anal 49(1):101–140

Bouchut F, Fernandez-Nieto ED, Mangeney A, Narbona-Reina G (2015b) A two-phase two-layer model for fluidized granular flows with dilatancy effects. J Fluid Mech (submitted)

Bouchut F, Fernandez-Nieto ED, Mangeney A, Narbona-Reina G (2016) A two-phase two-layer model for fluidized granular flows with dilatancy effects. J Fluid Mech 801:166–221

Boudon G, Le Friant A, Villemant B, Viode J-P (2005) Martinique. In Lindsay JM, Robertson REA, Shepherd JB, Shahiba A (eds) Volcanic atlas of the lesser antilles. Seismic Research Unit, University of the West Indies, Trinidad and Tobago, pp 127–146

Boudon G, Le Friant A, Komorowski J-C, Deplus C, Semet MP (2007) Volcano flank instability in the Lesser Antilles arc: diversity of scale, processes, and temporal recurrence. J Geophys Res 112:B08205. doi:10.1029/2006JB004674

Brunet M, Le Friant A, Boudon G, Lafuerza S, Talling P, Hornbach M, Ishizuka O, Lebas E, Guyard H, IODPExpedition340 Science party (2016) Composition, geometry and emplacement dynamics of a large volcanic island landslide offshore Martinique: from volcano flank-collapse to seafloor sediment failure? Geochem Geophys Geosyst. doi:10.1002/2015GC006034

Campbell CS, Cleary PW, Hopkins M (1995) Large-scale landslide simulations: global deformation, velocities and basal friction. J Geophys Res 100:8267–8273

Carracedo JC (1999) Growth, structure, instability and collapse of Canarian volcanoes and comparisons with Hawaiian volcanoes. J Volcanol Geotherm Res 94:1–19

Cassidy M, Trofimovs J, Watt SFL, Palmer MR, Taylor RN, Gernon TM, Talling PJ, Le Friant A (2012) Multi-stage collapse events in the South Soufrière Hills, Montserrat, as recorded in marine sediment cores. In: Wadge G, Robertson R, Voight B (eds) The eruption of Soufrière Hills volcano, Montserrat from 2000 to 2010. GB, Geological Society of London, London, pp 383–397

Delannay R, Valance A, Mangeney A, Roche O, Richard P (2016) Granular and particle-laden flows: from laboratory experiments to field observations. J Phys D Appl Phys (in press)

Denlinger RP, Iverson RM (2004) Granular avalanches across irregular three-dimensional terrain: 1. Theory and computation. J Geophys Res 109:F01014. doi:10.1029/2003JF000085

Deplus C, Le Friant A, Boudon G, Komorowski J-C, Villemant B, Harford C, Ségoufin J, Cheminée J-L (2001) Submarine evidence for large-scale debris avalanches in the Lesser Antilles arc. Earth Planet Sci Lett 192:145–157

Favreau P, Mangeney A, Lucas A, Crosta G, Bouchut F (2010) Numerical modeling of landquakes. Geophys Res Lett 37:L15305

Fernandez-Nieto E, Bouchut F, Bresch D, Castro-Diaz MJ, Mangeney A (2008) A new Savage–Hutter type model for submarine avalanches and generated tsunami. J Comp Phys 227(16):7720–7754

Garcia MO, Meyerhoff Hull D (1994) Turbidites from giant Hawaiian landslides: results from Ocean Drilling Program site 842. Geology 22:159–162

Germa A, Quidelleur X, Lahitte P, Labanieh S, Chauvel C (2011) The K–Ar Cassignol–Gillot technique applied to western Martinique lavas: a record of the evolution of the recent Lesser Antilles island arc activity from 2 Ma to Mount Pelée volcanism. Quat Geochronol 6:341–355

Giachetti T, Paris R, Kelfoun K, Pérez-Torrado FJ (2011) Numerical modelling of the tsunami triggered by the Güìmar debris avalanche, Tenerife (Canary Islands): comparison with field-based data. Mar Geol 284(1):189–202

Gittings ML (1992) 1992 SAIC's adaptive grid Eulerian Code. Defense nuclear agency numerical methods symposium, pp 28–30

Harbitz CB, Glimsdal S, Bazin S, Zamora N, Smebye HC, Løvholt F, Bungum H, Gauer P, Kjekstad O (2012) Tsunami hazard in the Caribbean: regional exposure derived from credible worst case scenarios. Cont Shelf Res 38:1–23

Harris JC, Grilli ST, Abadie S, Bakhsh TT (2012) Near-and far-field tsunami hazard from the potential flank collapse of the Cumbre Vieja Volcano. In: The 22nd international offshore and polar engineering conference. International Society of Offshore and Polar Engineers

Heinrich P, Boudon G, Komorowski JC, Sparks RSJ, Herd R, Voight B (2001a) Numerical simulation of the December 1997 debris avalanche in Montserrat. Geophys Res Lett 28(13):2529–2532

Heinrich P, Piatanesi A, Hebert H (2001b) Numerical modelling of tsunami generation and propagation from submarine slumps: the 1998 Papua-New Guinea event. Geophys J Int 144:97–111

Hibert C, Mangeney A, Grandjean G, Shapiro N (2011) Slopes instabilities in the Dolomieu crater, la Réunion island : from the seismic signal to the rockfalls characteristics. J Geophys Res Earth Surf 116:F04032

Hungr O (2008) Simplified models of spreading flow of dry granular material. Can Geotech J 45:1156–1168. doi:10.1139/T08-059

Hunt JE, Wynn RB, Masson DG, Talling PJ, Teagle DA (2011) Sedimentological and geochemical evidence for multistage failure of volcanic island landslides: a case study from Icod landslide on north Tenerife, Canary Islands. Geochem Geophys Geosyst 12(12):Q12007

Hunt JE, Wynn RB, Talling PJ, Masson DG (2013) Multistage collapse of eight western Canary Island landslides in the last 1.5 Ma: sedimentological and geochemical evidence from subunits in submarine flow deposits. Geochem Geophys Geosyst 14(7):2159–2181

Ionescu I, Mangeney A, Bouchut F, Roche O (2015) Viscoplastic modelling of granular column collapse with pressure and rate dependent viscosity. J NonNewton Fluid Mech 219:1–18

Iverson RM, George DL (2014) A depth-averaged debris flow model that includes the effects of evolving dilatancy. I. Physical basis. Proc R Soc A 470:20130819

Kelfoun K (2011) Suitability of simple rheological laws for the numerical simulation of dense pyroclastic flows and long—runout volcanic avalanches. J Geophys Res Solid Earth 116:b08209. doi:10.1029/2010JB007622

Kelfoun K, Vargas SV (2015) VolcFlow capabilities and perspectives of development for the simulation of lava flows. In: Harris AJL, De Groeve T, Garel F, Carn SA (eds) Detecting, modelling and responding to effusive eruptions. Geological Society, London, Special Publications, London p 426

Labazuy P (1996) Recurrent landslides events on the submarine flank of Piton de la Fournaise volcano (Reunion Island). In: McGuire WJ, Jones AP, Neuberg J (eds) Volcano instability on the Earth and other planets, vol. 110, Geol. Soc. Spec. Publ., London, pp 295–306. doi: 10.1144/GSL.SP.1996.110.01.23

Le Friant A, Boudon G, Deplus C, Villemant B (2003a) Large scale flank collapse events during the activity of Montagne Peléee, Martinique, Lesser Antilles. J Geophys Res 108(B1):2055. doi:10.1029/2001JB001624

Le Friant A, Heinrich P, Deplus C, Boudon G (2003b) Numerical simulation of the last flank collapse event of Montagne Pelée, Martinique, Lesser Antilles. Geophys Res Lett 30(2):1034. doi:10.1029/2002GL015903

Le Friant A, Lebas E, Clément V, Boudon G, Deplus C, de Voogd B, Bachèlery P (2011) A new model for the evolution of la Réunion volcanic complex from complete geophysical surveys. Geophys Res Lett. doi:10.1029/2011GL047489

Le Friant A, Ishizuka O, Stroncik NA, The Expedition 340 Scientists (2013). In: Proceedings of integrated ocean drilling program, 340, Integrated Ocean Drill. Program Manage. Int. Inc., Tokyo. doi:10.2204/iodp.proc.340.2013

Le Friant A et al (2015) Submarine record of volcanic island construction and collapse in the Lesser Antilles arc: first scientific drilling of submarine volcanic island landslides by IODP Expedition 340. Geochem Geophys Geosyst. doi:10.1002/2014GC005652

Legros F (2002) The mobility of long-runout landslides. Eng Geol 63:301–331

Levy C, Mangeney A, Bonilla F, Hibert C, Calder ES, Smith PJ (2015) Friction weakening in granular flows deduced from seismic records at the Soufrière Hills Volcano, Montserrat. J Geophys Res Solid Earth 120(11):7536–7557

Lucas A, Mangeney A, Ampuero JP (2014) Frictional velocity-weakening in landslides on earth and on other planetary bodies. Nature Commun 5:3417

Mangeney A, Heinrich Ph, Roche R, Boudon G, Cheminée JL (2000) Modeling of debris avalanche and generated water waves: application to real and potential events in Montserrat. Phys Chem Earth 25(9–11):741–745

Mangeney A, Bouchut F, Thomas N, Vilotte J, Bristeau M (2007) Numerical modeling of self-channeling granular flows and of their levee-channel deposits. J Geophys Res 112:F02017

Mangeney-Castelnau A, Vilotte JP, Bristeau MO, Perthame B, Bouchut F, Simeoni C, Yernini S (2003) Numerical modeling of avalanches based on Saint-Venant equations using a kinetic scheme. J Geophys Res 108(B11):2527

Mangeney-Castelnau A, Bouchut F, Vilotte J, Lajeunesse E, Aubertin A, Pirulli M (2005) On the use of saint venant equations to simulate the spreading of a granular mass. J Geophys Res 110:B09103

Masson DG, Watts AB, Gee MJR, Urgeles R, Mitchell NC, Le Bas TP, Canals M (2002) Slope failures on the flanks of the western Canary Islands. Earth Sci Rev 57:1–35

McGuire WJ (1996) Volcano instability: a review of contemporary themes. In: McGuire WJ et al (ed) Volcano instability on the earth and other planets, vol. 110, Geological Society Special Publication, London, pp 1–23. doi:10.1144/GSL.SP.1996.110.01.01

Moore JG, Clague DA, Holcomb RT, Lipman PW, Normark WR, Torresan ME (1989) Prodigious submarine landslides on the Hawaiian ridge. J Geophys Res 94:17465–17484

Moore JG, Normark WR, Holcomb RT (1994) Giant Hawaiian landslides. Annu Rev Earth Planet Sci 22(119–144):1994

Moretti L, Mangeney A, Capdeville Y et al (2012) Numerical modeling of the Mount Steller landslide flow history and of the generated long period seismic waves. Geophys Res Lett 39:L16402

Moretti L, Allstadt K, Mangeney A, Capdeville Y, Stutzmann E, Bouchut F (2015) Numerical modeling of the Mount Meager landslide constrained by its force history derived from seismic data. J Geophys Res Solid Earth 120(4):2579–2599

Oehler JF, Lenat JF, Labazuy P (2008) Growth and collapse of the Reunion Island volcanoes. Bull Volcanol 70:717–742. doi:10.1007/s00445-007-0163-0

Pailha M, Pouliquen O (2009) A two-phase flow description of the initiation of underwater granular avalanches. J Fluid Mech 633:115–135

Pelanti M, Bouchut F, Mangeney A (2008) Roe-type scheme for two-phase shallow granular flows over variable topography. ESAIM Math Model Num Anal 42:851–885

Pirulli M, Mangeney A (2008) Result of back-analysis of the propagation of rock avalanches as a function of the assumed Rheology. Rock Mech Rock Eng 41(1):59–84

Pitman EB, Le L (2005) A two-fluid model for avalanche and debris flows. Phil Trans R Soc A 363:1573–1601

Pouliquen O (1999) Scaling laws in granular flows down rough inclined planes. Phys Fluids 11:542–548

Pouliquen O, Forterre Y (2002) Friction law for dense granular flows: application to the motion of a mass down a rough inclined plane. J Fluid Mech 453:133–151

Pudasaini SP, Hutter K (2007) Avalanche dynamics: dynamics of rapid flows of dense granular avalanches. Springer, Berlin

Rondon L, Pouliquen O, Aussillous P (2011) Granular collapse in a fluid: role of the initial volume fraction. Phys Fluids 23:073301

Savage SB, Hutter K (1989) The motion of a finite mass of granular material down a rough incline. J Fluid Mech 199:177–215

Schneider D, Bartelt P, Caplan-Auerbach J, Christen M, Huggel C, McArdell BW (2010) Insights into rock–ice avalanche dynamics by combined analysis of seismic recordings and a numerical avalanche model. J Geophys Res 115:F04026

Siebert L (1984) Large volcanic debris avalanches: characteristics of source areas, deposits, and associated eruptions. J Volcanol Geotherm Res 22:163–197

Viroulet S, Sauret A, Kimmoun O (2014) Tsunami generated by a granular collapse down a rough inclined plane. Europhys Lett 105:34004

Voight B, Komorowski JC, Norton GE et al (2002) The 26 December (Boxing day) 1997 sector collapse and debris avalanche at Soufrière Hills Volcano, Montserrat. In: Druitt TH, Kokelaar BP (eds) The eruption of Soufrie‘re Hills Volcano, Montserrat, from 1995 to 1999. Geological Society, London, Memoirs, 21, pp 363–407

Wynn RB, Masson DG (2003) Canary Islands landslides and tsunami generation: can we use turbidite deposits to interpret landslide processes? In: Locat J, Mienert J (eds), Submarine mass movements and their consequences, Kluwer Academic Publ., Boston, London, pp 325–332

Yamada M, Mangeney A, Matsushi Y, Moretti L (2016) Estimation of dynamic friction process of the Akatani landslide based on the waveform inversion and numerical simulation Geophys J Int (accepted)